Fundamentals of Curvilinear Ferromagnetism: Statics and Dynamics of Geometrically Curved Wires and Narrow Ribbons

Denis D. Sheka,* Oleksandr V. Pylypovskyi,* Oleksii M. Volkov, Kostiantyn V. Yershov, Volodymyr P. Kravchuk, and Denys Makarov*

Low-dimensional magnetic architectures including wires and thin films are key enablers of prospective ultrafast and energy efficient memory, logic, and sensor devices relying on spin-orbitronic and magnonic concepts. Curvilinear magnetism emerged as a novel approach in material science, which allows tailoring of the fundamental anisotropic and chiral responses relying on the geometrical curvature of magnetic architectures. Much attention is dedicated to magnetic wires of Möbius, helical, or DNA-like double helical shapes, which act as prototypical objects for the exploration of the fundamentals of curvilinear magnetism. Although there is a bulk number of original publications covering fabrication, characterization, and theory of magnetic wires, there is no comprehensive review of the theoretical framework of how to describe these architectures. Here, theoretical activities on the topic of curvilinear magnetic wires and narrow nanoribbons are summarized, providing a systematic review of the emergent interactions and novel physical effects caused by the curvature. Prospective research directions of curvilinear spintronics and spin-orbitronics are discussed, the fundamental framework for curvilinear magnonics are outlined, and mechanically flexible curvilinear architectures for soft robotics are introduced.

1. Introduction

Since the onset of nanosciences and nanotechnologies, the influence of the geometry of an object on the order parameter became an important topic of fundamental research. Starting with studies in quantum mechanics, the transport properties of quantum-mechanical particles constrained to a curved wire were found to be affected by the geometrical curvature and torsion, which are encoded in the quantum geometrical scalar[1,2] and vector[3,4] potentials. They cause a vast of intriguing phenomena at the nanoscale including topological band structure of electrons bound to periodic minimal surfaces,[5] winding-generated bound states in spirally rolled-up nanotubes,[6] torsion generated confinement of electron by the spin-orbit coupling in a nanoscale helical wire,[3] with some of these effects resulting in a chiral symmetry breaking.[3] Much attention is dedicated also to superconductivity in curved geometries.[7–9] Especially for chiral superconductors, where the physical implications of the geometric curvature results in the geometric Josephson effects, geometry-based superconducting quantum interference devices and radiators.[10] Curvilinear and 3D mesoscale systems are actively explored in other disciplines including quantum systems,[3,11] semiconductors (not only fundamental research but also current transistor technologies),[12–14] Dirac materials,[15,16] photonics,[17–19] and plasmonics[20–22] for intra-chip multilevel communication[23] as well as in liquid crystals,[24–26] microrobotics,[27–29] and magnetism.[30]

Curvilinear magnetism encompasses a range of effects of geometrical curvature on magnetic responses of low-dimensional

D. D. Sheka
Faculty of Radiophysics, Electronics and Computer Systems
Taras Shevchenko National University of Kyiv
Kyiv 01601, Ukraine
E-mail: sheka@knu.ua

O. V. Pylypovskyi, O. M. Volkov, D. Makarov
Helmholtz-Zentrum Dresden - Rossendorf e.V.
Institute of Ion Beam Physics and Materials Research
01328 Dresden, Germany
E-mail: o.pylypovskyi@hzdr.de; d.makarov@hzdr.de

⬭ The ORCID identification number(s) for the author(s) of this article can be found under https://doi.org/10.1002/smll.202105219.

O. V. Pylypovskyi
Kyiv Academic University
Kyiv 03142, Ukraine

K. V. Yershov
Leibniz-Institut für Festkörper- und Werkstoffforschung
IFW Dresden, 01171 Dresden, Germany

V. P. Kravchuk
Institut für Theoretische Festkörperphysik
Karlsruher Institut für Technologie
76131 Karlsruhe, Germany

K. V. Yershov, V. P. Kravchuk
Bogolyubov Institute for Theoretical Physics of National
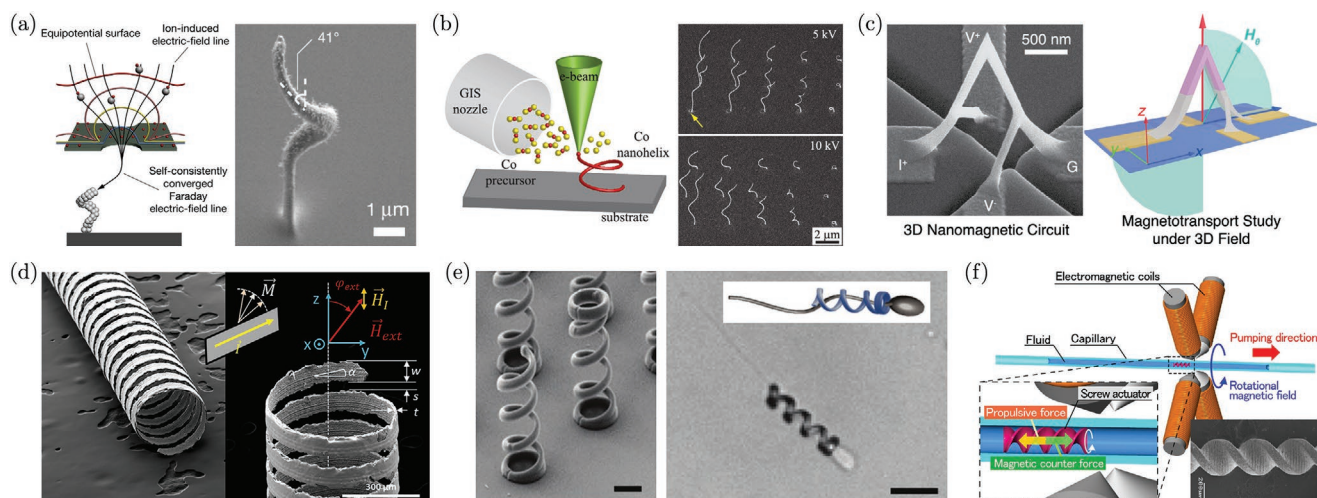Academy of Sciences of Ukraine
Kyiv 03142, Ukraine

**ADVANCED
SCIENCE NEWS**

www.advancedsciencenews.com

NANO · MICRO

small

www.small-journal.com

Figure 1. Curvilinear wires and stripes. a) Schematic illustration of nanohelices fabrication via charged aerosol particles by means of guiding electric-field lines together with nanostage rotation.[43] Adapted with permission.[43] Copyright 2021, Springer Nature. This novel method enables various nanoobject fabrication in a dry atmosphere and could be substituted or supplemented by glancing angle deposition, which employs oblique angle deposition and substrate rotation.[45,69,70] Due to their shapes and sizes, these nanoobjects find application as nano-propellers for noninvasive biomedical applications.[44,71,72] Furthermore, they are used as elements for magneto-chiral dichroism of light by providing the direct coupling between the structural chirality, magnetic state, and light absorption.[46] b) Schematic of the Co nanohelices fabricated using FEBID.[52] Reproduced with permission.[52] Copyright 2020, American Chemical Society. This object allows for the geometrical control of magnetic chirality and can be used to stabilize and experimentally investigate topologically non-trivial magnetic textures.[49,52,57,73,74] c) Ferromagnetic nanobridge with contacts fabricated by means of FEBID for 3D spintronics.[56] Reproduced under the terms of the Creative Commons license.[56] Copyright 2021, The Author(s), Published by American Chemical Society. d) Chiral anisotropic magnetoresistance of ferromagnetic microhelices fabricated by means of electroforming.[75] Reproduced with permission.[75] Copyright, AIP Publishing. The helical geometry imprints a characteristic angular dependence of the anisotropic magnetoresistance effect due to the misalignment of the magnetic texture and the external magnetic field. e) Magnetic helices prepared by two-photon absorption printing enable new approaches for artificial fertilization.[76] Adapted with permission.[76] Copyright 2017, Wiley-VCH. An immobile sperm cell is captured by a remotely controlled magnetic helix and delivered to the oocyte for fertilization.[76,77] f) A prototype for a microfluidic pump based on magnetic microscrews fabricated by micro-stereolithography.[78] To pump liquids, the microscrew is positioned inside a microcapillary and controlled by means of rotating magnetic fields. Reproduced with permission.[78] Copyright 2009, IEEE.

magnetic architectures whose geometry follows planar or space curves in 3D. This includes curved thin wires (1D magnetic systems, 1D), narrow ribbons, and thin shells (2D magnetic systems, 2D). In this manuscript, we will refer to the magnetic dimensionality of the objects, while geometrically they are immersed in 3D space. The rigorous micromagnetic theory of the curvilinear magnetism for curved magnetic thin films was formulated by ref. [31] in 2014 for local interactions (exchange and anisotropy) and extended to the strict micromagnetic theory by ref. [32] in 2020 (local and nonlocal magnetostatic interactions). These works demonstrated that the fundamental anisotropic and chiral responses of magnetic thin films can be tailored relying on extrinsic parameters, namely on local curvatures. This possibility was recognized by the community as a novel approach to the material science, which allows to decouple the optimization of the intrinsic material properties from the tuning of the responses as needed for applications. The topic of curvilinear magnetism is highlighted in the 2017 Magnetism Roadmap,[33] Section 3] and 2020 Magnetism Roadmap,[34] Section 3]. The current activities on the curvilinear thin films are summarized in numerous reviews.[30,35–41]

At the moment, the fundamental research in the field of curvilinear magnetism is focused on curved wires and stripes. This reason for this is threefold: i) The mathematical framework for the description of the curvilinear effects is way simpler for the case of 1D magnetic systems, yet it contains all important ingredients including emergent anisotropic and

chiral interactions, chiral symmetry breaking, and magnetization patterning, which are also predicted for more complex curvilinear geometries, like curved thin films. ii) The theoretically predicted geometry-induced chiral effects were experimentally confirmed by ref. [42] in 2019 in parabolic stripes of achiral Permalloy. iii) The community developed experimental methods, which allow to fabricate complex 3D magnetic wires with a nanometer scale spatial resolution via charged aerosol particles guided with electrostatic lens,[43] glancing angular deposition,[44–46] focused electron beam induced deposition (FEBID)[37,47–52] or implosion nanofabrication including a combination of two-photon lithography and electrodeposition.[53] By using these methods, it is possible to fabricate complex magnetic wireframe structures,[53–56] magnetic nanohelices[45,52,57] (**Figure 1**), magnetic Möebius ring at the nanoscale,[58] magnetic knots,[59] magnetic DNA-like double helices[57] to name just a few appealing geometries.

These intense activities on the fabrication and characterization of curvilinear magnetic wires do require a solid theoretical foundation for the easy and intuitive interpretation of the experimental results. At the moment, there is no comprehensive review of curvilinear effects in curvilinear 1D magnetic wires, which can consolidate and guide experimental exploration in this new research field. Instead, there are numerous original papers on the curvature effects in 1D wires and ribbons, which are written for experts and are focused on very specific aspects missing to deliver the full picture.

ADVANCED
SCIENCE NEWS
www.advancedsciencenews.com

NANO · MICRO
small
www.small-journal.com

The objective of this work is to provide a critical review of the state of the art in the theoretical understanding of the curvilinear magnetism of nanowires and nanoribbons. The review summarizes in an accessible manner the complex theoretical ideas on the emergent interactions and physical effects caused by the geometrical curvature in 1D magnetic wires. In brief, we will systematically describe in the micromagnetic theory of curvilinear wires[60] and ribbons[61] and then proceed with the description of curved helimagnetic wires,[62] curvilinear spintronics,[63] curvilinear spin-orbirtonics,[64] curvilinear magnonics,[65,66] and mechanically flexible (helimagnetic) wires.[67,68] Methodologically, we put efforts to unify the terminology and mathematical notation to simplify the understanding of the topic and make it accessible as well for the young generation of scientists, who only considers joining this new field of research in modern magnetism.

2. Emergent Interactions in Curvilinear Wires and Narrow Ribbons

Magnetic responses of curvilinear magnets are enriched by new physical effects stemming from the mutual interplay between the geometrical properties of the underlying substrate and the magnetic texture. The effects are described based on the geometry-governed emergent magnetic interactions caused by the local and global properties of the object's geometry. In this respect, local geometric properties of thin wires, namely curvature and torsion uniquely determine the shape of the wire and are crucial for the understanding of the modification of the local magnetic interactions, in particular, exchange interaction, magneto-crystalline anisotropy, and Dzyaloshinskii–Moriya interaction (DMI). The impact of local geometrical properties on the magnetic texture is, for example, in the selection of the chirality of the domain wall and its pinning. Furthermore, we would like to emphasize on the importance of the closeness of a curve as a global geometrical parameter. This property has influence on the formation of the overall magnetic pattern. For instance, closeness of a curve requires smoothness of the magnetic texture in confined space. Relevant examples are the presence of vortex and onion states in a ring geometry or, more generally, the necessity to accommodate an even number of domain walls in any closed curve. The only nonlocal magnetic interaction in ferromagnets, namely the magnetostatic interaction, in its main order can be reduced to the biaxial anisotropy for the case of ultrathin wires.[61,79] Nonlocal magnetostatic effects in ultrathin wires are in the fourth order and are typically neglected. Therefore, in the following, we focus our discussion only on the local magnetic effects in curvilinear wires and narrow ribbons. The common feature for these two systems is the one-dimensionality of the magnetization, which depends only on one coordinate along the wire axis or ribbon central curve. In this respect, both these systems are mathematically described as being 1D. Still, the difference between these two geometries is that the rectangular cross-section of the ribbon results in the necessarily biaxial shape anisotropy, see Section 2.3. At the same time, the shape anisotropy of the wire is uniaxial oriented along the wire axis, see Section 2.1.

2.1. Curvilinear Wires

A unified description of the curvature–induced effects is based on a micromagnetic framework of curvilinear magnetism.[31,32,60] Here, we focus on an uniaxial ferromagnet with the following energy

$$E[\boldsymbol{m}] = \int d\boldsymbol{r} \left(\mathcal{E}^A + \mathcal{E}^X + \mathcal{E}^D \right) \tag{1}$$

The energy functional (1) contains the exchange energy density $\mathcal{E}^X$ and the energy density of the intrinsic DMI $\mathcal{E}^D$. The symmetry and strength of the DMI term is determined by the crystal structure and/or properties of the layer stack.[80–83] The term $\mathcal{E}^A = -K(\boldsymbol{m} \cdot \boldsymbol{e}_A)^2$ is the anisotropy energy density with K being the anisotropy constant, $\boldsymbol{e}_A$ being the anisotropy axis, $\boldsymbol{m} = \boldsymbol{M}/M_s$ being the normalized magnetization, and M_s being the saturation magnetization. The anisotropy is of easy-axis or hard-axis type for $K > 0$ and $K < 0$, respectively. It is important to emphasize that the anisotropy is the enabler of the geometry-governed magnetic interactions because this is the only energy term, which follows the sample geometry. In ferromagnets, anisotropy has two primary origins, spin-orbit and dipolar interactions. Macroscopically, they are described as the magneto-crystalline and interfacial anisotropy as well as magnetostatics. The possibility to reduce the nonlocal magnetostatics to the local anisotropic interaction was rigorously demonstrated for curvilinear wires in ref. [79] and curvilinear ribbons in ref. [61]. We note that due to its smallness (fourth order), the non-local part of the magnetostatic interaction can be neglected for ultrathin wires. This is in stark contrast to thin shells, where it is known that the nonlocal magnetostatics is responsible for nonlocal chiral effects.[32] The local part of the magnetostatic interaction in ultrathin wires induces the shape anisotropy, with the axis $\boldsymbol{e}_A = \boldsymbol{e}_A(\boldsymbol{r})$ following the sample geometry. We note that magnetostatics induces anisotropy easy axis only along the tangential direction. The magneto-crystalline or interface anisotropy provides additional means to define the anisotropy axis $\boldsymbol{e}_A$. For instance, interfacial anisotropy in Co/Pt multilayers was used to stabilize radially magnetized helical coil structures.[84] Other sources of anisotropy like strain can be used to tailor the orientation of the anisotropy axis.

For the case of tangential anisotropy, the anisotropy coefficient K incorporates the magneto-crystalline anisotropy with the coefficient K^{mc} and the magnetostatic contribution. In the case of thin curved wires of circular (or square) cross-section, the effective anisotropy constant $K = K^{mc} + \pi M_s^2$.[79] The pure dipolar interaction in a chain of classical spins mimics the anisotropy as well.[85] Here, the anisotropy energy per unit length of a curvilinear spin chain reads $K_d = 3\zeta(3) \times (2\mu_B S)^2 / a^4$, where $\zeta(\bullet)$ is the Riemann zeta-function, μ_B is the Bohr magneton, S is the dimensionless spin length, and a is the distance between neighboring spins. This approach is valid for $\kappa, |\tau| \ll 1/a$.[86]

To ease the understanding of the behavior of a geometrically curved system, it is insightful to make a coordinate transformation into a curvilinear reference frame, which follows the sample geometry with one of the curvilinear basis vector being determined by $\boldsymbol{e}_A(\boldsymbol{r})$. This provides means to recover the translation invariance of the effective anisotropy.[31,60] We consider a ferromagnetic wire defined as a space domain

$r = \gamma(s) + \xi_1 e_N + \xi_2 e_B$. Here, the central curve $\gamma(s)$ is parameterized by the arc length s. The perpendicular cross-section, parameterized by ξ_1 and ξ_2 is defined by the normal and binormal vectors e_N and e_B, respectively. The relation between the normal and binormal directions can be introduced using the TNB (Tangential–Normal–Binormal) frame[87]

$$e_T = \gamma', \qquad e_N = \frac{e_T'}{|e_T'|}, \qquad e_B = e_T \times e_N \qquad (2a)$$

where prime denotes the derivative with respect to the arc length s and e_T is the tangential unit vector. The local TNB-basis is spatially inhomogeneous, with all unit vectors being functions of s. The differential properties of γ are determined by the Frenet equations[87,88] (also known as the Frenet–Serret equations[89])

$$e_\alpha' = \mathcal{F}_{\alpha\beta} e_\beta, \qquad \|\mathcal{F}_{\alpha\beta}\| = \begin{pmatrix} 0 & \kappa & 0 \\ -\kappa & 0 & \tau \\ 0 & -\tau & 0 \end{pmatrix} \qquad (2b)$$

with κ and τ being the curvature and torsion, respectively, and Greek indices enumerating curvilinear coordinates, $\alpha, \beta = $ T, N, B. It is commonly accepted that for 3D wires $\kappa \geq 0$ and τ are alternating-sign functions. The model (2) is also valid for planar curves with $\tau \equiv 0$ and oriented (alternating-sign) curvature κ.[87]

The current theory of curvilinear 1D magnetism is based on the assumption that the wire has a circular cross-section with a constant thickness h and the anisotropy directions e_A do not vary along the thickness. In this case, the magnetization texture can be considered as being uniform along the cross-section. This assumption is valid if the sample thickness does not exceed several times the characteristic magnetic length scale ℓ. A varying thickness even along a straight wire significantly

alters magnetic textures[90] via magnetostatics and should be addressed in curvilinear systems separately. Furthermore, we consider wires with a small cross-section (thickness $h \ll 1/\kappa$, $1/\tau$[60]), which do not support transversal magnetic textures. This means that the existing theory is not suitable for the description of 3D topological defects such as Bloch points, chiral bobbers, hopfions.[91] For details on these systems, we refer to the monograph[92] and references therein. In this way, we arrive in the assumption of the magnetization one-dimensionality with $m = m(s)$ (m does not depend on the coordinate ξ_2 and ξ_3).[60] These are the limitations, which determine the applicability of the stat-of-the-art theory of curvilinear 1D magnetic wires.

2.2. Emergent Mesoscale Interactions: DMI and Anisotropy

The local inversion symmetry of magnet interactions becomes broken geometrically in curved systems.[35] Therefore, it is natural to restructure all energy terms in Equation (1), which contain spatial derivatives. For this purpose, it is useful to link the reference frame to the curvilinear geometry of the object (2), see **Figure 2**a. This transformation allows to take into account the spatial variation of the anisotropy and recover the translation invariance of the anisotropy energy density.[60,61] A characteristic example is the exchange interaction: being isotropic in the Cartesian reference frame, it contains components of different symmetries in curvilinear coordinates[60]

$$\mathcal{E}^x = (m_\alpha e_\alpha)'(m_\beta e_\beta)' = \mathcal{E}_0^x + \mathcal{E}_A^x + \mathcal{E}_D^x,$$
$$\mathcal{E}_0^x = A m_\alpha' m_\alpha', \quad \mathcal{E}_A^x = K_{\alpha\beta}^x m_\alpha m_\beta, \quad \mathcal{E}_D^x = D_{\alpha\beta}^x (m_\alpha m_\beta' - m_\alpha' m_\beta) \qquad (3)$$

with A being exchange stiffness, $D_{\alpha\beta}^x = A\mathcal{F}_{\alpha\beta}$ and $K_{\alpha\beta}^x = A\mathcal{F}_{\alpha\gamma}\mathcal{F}_{\beta\gamma}$, and the Einstein summation convention is
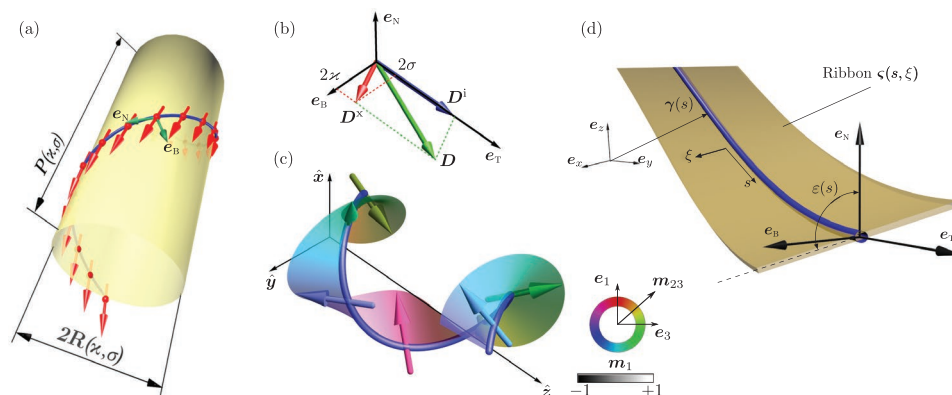

Figure 2. Curvilinear wires and ribbons. a) A helix-shaped wire of radius R and pitch P wrapped around a cylinder. The magnetization is shown with red arrows, TN unit vectors are indicated in green. Adapted under the terms of the CC BY Creative Commons Attribution 4.0 International License (http://creativecommons.org/licenses/by/4.0/).[64] Copyright 2016, Springer Nature. b) The concept of the mesoscale DMI: intrinsic DMI vector (blue arrow, D^i), extrinsic DMI stemming from the exchange interaction (red arrow, D^x) and the resulting mesoscale DMI vector (green arrow, D) are shown in the TNB reference frame. Dimensionless curvature ($\varkappa = \kappa\ell$) and torsion ($\sigma = \tau\ell$) of the helical wire are shown as well. Adapted under the terms of the CC-BY Creative Commons Attribution 4.0 International license (https://creativecommons.org/licenses/by/4.0).[93] Copyright 2018, The Author(s), Published by Springer Nature. c) Elliptical helicoidal magnetic state on a helix wire determined by the mesoscale DMI. Colors of the magnetization vectors and covering surface shows the direction of the m in rotated ψ-frame, see Equation (26). Reproduced under the terms of the CC-BY Creative Commons Attribution 4.0 International license (https://creativecommons.org/licenses/by/4.0).[93] Copyright 2018, The Author(s), Published by Springer Nature. d) The geometry of the narrow ribbon ς (yellow surface) is determined by the rotation of the line segment about the central curve γ (blue line). The rate of rotation of the line segment is given by the function $\varepsilon(s)$. Reproduced with permission.[6] Copyright 2017, IOP Publishing.

used. In the local reference frame, the exchange interaction is split in three terms, with one resembling the common nonuniform exchange $\mathcal{E}_0^x$ and two additional geometry-governed contributions: emergent biaxial anisotropy $\mathcal{E}_A^x$ and emergent DMI $\mathcal{E}_D^x$. In contrast to the crystalline or interfacial spin-orbit driven DMI, the emergent DMI term stems from the exchange interaction and depends on the object geometry. In this way, it is extrinsic to the crystal structure and can be manipulated by the object geometry. The anisotropy term $\mathcal{E}_A^x$ is bilinear with respect to the curvature and torsion. It is similar to the geometric potential experienced by an electron in a curved quantum wire:[94] the coefficients $K_{\alpha\beta}$ play the role of the effective anisotropy coefficients, induced by the curvature and torsion of the wire. The symmetry of the emergent DMI is determined by the antisymmetric Frenet tensor (2b), which contains the curvilinear analogue of the Lifshitz invariants, $m_\alpha m_\beta' - m_\alpha' m_\beta$. Hence, for a curvilinear 1D wire, the chiral interaction is determined by the vector of the extrinsic DMI D^x, $D_\alpha^x = \varepsilon_{\alpha\beta\gamma} D_{\beta\gamma}^x$:

$$\mathcal{E}_D^x = \varepsilon_{\alpha\beta\gamma} D_\alpha^x m_\beta m_\alpha', \qquad D^x = 2A(e_T \tau + e_B \kappa) \tag{4}$$

with $\varepsilon_{\alpha\beta\gamma}$ being the permutation symbol.[88]

As the magnetization is described by the unit vector m, it is convenient to use its angular parametrization. An appropriate choice of the reference axes of the polar and azimuthal angles is dependent on the symmetry of the given problem. To describe the ground state in planar curved wires[60,62,95] and spin waves in wires along space curves,[65,66] it is suitable to use the expression $m_{BT} = e_T \sin\Theta\cos\Phi + e_N \sin\Theta\sin\Phi + e_B \cos\Phi$, where Θ characterizes the deviation from the binormal direction and Φ describes the deviation from the tangential direction in the osculating TN plane. Then the exchange energy (3) reads[60]

$$\mathcal{E}^x[m_{BT}] = A(\Theta' - \tau\sin\Phi)^2 + A\big[\sin\Theta(\Phi' + \kappa) - \tau\cos\Theta\cos\Phi\big]^2 \tag{5}$$

This formulation allows to have the defined azimuthal angle Φ in the case of the strictly tangential magnetization $m = e_T$ with the magnetization angles $\Theta = \pi/2$ and $\Phi = 0$. However, for the description of domain walls,[64,95] it is convenient to measure the polar angle from the anisotropy axis using $m_{TN} = e_T\cos\theta + e_N\sin\theta\cos\phi + e_B\sin\theta\sin\phi$, where the polar angle θ is the deviation of the magnetization from the direction, which is tangential to the curve, while the azimuthal angle ϕ corresponds to the deviation from the normal direction in the normal NB plane. The strictly tangential magnetization distribution in this parametrization is described by $\theta = 0$. Then, the exchange energy reads[60]

$$\mathcal{E}^x[m_{TN}] = A(\theta' + \kappa\cos\phi)^2 + A\big[\sin\theta(\phi' + \tau) - \kappa\cos\theta\sin\phi\big]^2 \tag{6}$$

The comparison of expressions (5) and (6) shows that the curvature $\kappa \neq 0$ can be the source of inhomogeneous m_T component via azimuthal angle, while the torsion $\tau \neq 0$ in the same way can influence on m_B. We note that introducing these two parametrizations is motivated by the idea to simplify the specific physical analysis. Otherwise, mathematically, these two parametrizations are related by the rotation operation.

We proceed with the discussion of the intrinsic DMI term in the model (1), which reads[83,96]

$$\mathcal{E}^D = D^i \cdot [m \times m'] \tag{7}$$

with D^i being the vector of the intrinsic DMI. The coordinate-independent expression (7) for the energy density of the intrinsic DMI preserves its form as well for curvilinear wires[93] with $D^i = e_T D_T^i + e_N D_N^i + e_B D_B^i$. Similar to the case of the exchange energy, the intrinsic DMI can be decomposed in two components with different symmetries. The first one contains the curvilinear analogue of Lifshitz invariants, which is the regular part of the intrinsic DMI. Besides, there appears an emergent biaxial anisotropy, stemming from the intrinsic DMI.

Then, the total energy density in the local reference frame can be written[93]

$$\mathcal{E} = \mathcal{E}_0^x + D_{\alpha\beta}(m_\alpha m_\beta' - m_\beta m_\alpha') + K_{\alpha\beta} m_\alpha m_\beta \tag{8}$$

with $D_{\alpha\beta}$ and $K_{\alpha\beta}$ being antisymmetric and symmetric tensors of the mesoscale DMI and anisotropy, incorporating contributions of both geometry–induced and intrinsic energy terms. The mesoscale DMI tensor reads[93]

$$\|D_{\alpha\beta}\| = \left\| \begin{matrix} 0 & \dfrac{2A\kappa + D_B^i}{2} & D_N^i \\[2ex] -\dfrac{2A\kappa + D_B^i}{2} & 0 & \dfrac{2A\tau + D_T^i}{2} \\[2ex] -D_N^i & -\dfrac{2A\tau + D_T^i}{2} & 0 \end{matrix} \right\| \tag{9a}$$

see Figure 2b,c. The corresponding energy term can also be presented in the vector form of $\mathcal{E}^{mD} = \varepsilon_{\alpha\beta\gamma} D_\alpha m_\beta m_\gamma'$ similar to Equation (7) with the mesoscale DMI vector[93]

$$D = D^i + D^x = e_T(2A\tau + D_T^i) + e_N D_N^i + e_B(2A\kappa + D_B^i) \tag{9b}$$

which is now determined by both material and geometrical properties of the wire. Note, that the mesoscale DMI contains the full set of Lifshitz invariants possible in 1D systems. The DMI forces the magnetization vector to experience a spatial rotation in the plane, perpendicular to D. Therefore, one can expect the appearance of different spiral textures depending on the strength of the mesoscale DMI, D.

The tensor of the total anisotropy, which includes the intrinsic and geometry–induced terms, reads[93]

$$\|K_{\alpha\beta}\| = \left\| \begin{matrix} -K - A\kappa^2 + \tau D_T^i & \dfrac{\tau D_N^i}{2} & \dfrac{\kappa D_T^i + \tau D_B^i}{2} - A\kappa\tau \\[2ex] \dfrac{\tau D_N^i}{2} & A(\kappa^2 + \tau^2) & \dfrac{\kappa D_N^i}{2} \\[2ex] \dfrac{\kappa D_T^i + \tau D_B^i}{2} - A\kappa\tau & \dfrac{\kappa D_N^i}{2} & -A\tau^2 + \kappa D_B^i \end{matrix} \right\| \tag{9c}$$

The contribution from the intrinsic DMI to the anisotropy tensor results in the absence of zero components of $K_{\alpha\beta}$, see Equation (9c). This differs from the contribution from the

ADVANCED
SCIENCE NEWS
www.advancedsciencenews.com

NANO · MICRO
small
www.small-journal.com

exchange energy (3). The principal axes of the anisotropy determining the easy plane and easy axis of the magnetization are given by the diagonalization of the matrix (9c), which can be characterized by the rotation of the reference frame by a certain angle ψ in 3D space. In the following, we refer to the reference frame aligned with the principal axes of the anisotropy as the ψ-frame. In the particular case of $D_N^i = 0$, the easy plane coincides with the rectifying TB plane given by the tangential and binormal unit vectors. The easy axis is tilted from the tangential direction by the angle ψ.

2.3. Curvilinear Narrow Ribbons

Above we discussed the micromagnetic framework of curved thin wires of circular cross-section (1D magnetic system). This framework can be extended to describe a thin and narrow ribbon, which is a stripe of rectangular cross-section swept out by a line segment, turning as it moves along the central curve γ. We will see that the micromagnetic properties of a narrow ribbon can be reduced to that of a 1D magnetic wire with biaxial anisotropy and DMI. The geometry of the ribbon is different from γ. The curvature and torsion of the wire are spatially modulated and derived from the geometry of γ accounting for the rate of turning of the line segment. We note that while the ribbon is geometrically created as a part of a 2D surface, magnetically it is described as a 1D system.

We consider a narrow ribbon of width w and thickness h assuming[61]

$$\left(\frac{w}{\ell}\right)^2 \le \frac{h}{\ell} \ll \frac{w}{\ell} \ll 1 \lesssim \frac{L}{\ell} \tag{10}$$

with L being the length of the ribbon and $\ell = \sqrt{A/K}$ being a typical length scale, the so-called magnetic length. Then the ribbon can be defined as a 2D surface without self-intersections swept out by a line segment centered at and perpendicular to γ, moving and possibly turning along γ:[97]

$$\varsigma = \gamma(s) + e_N(s)\xi \cos \varepsilon(s) + e_B(s)\xi \sin \varepsilon(s) \tag{11}$$

with $\xi \in [-w/2, w/2]$ and $\varepsilon(s)$ determining the orientation of the line segment with respect to the normal and binormal directions, see Figure 2d. Then, the reference frame within ς is given as

$$e_\mu = \frac{\partial_\mu \varsigma}{|\partial_\mu \varsigma|}, \quad \mu = s, \xi, \quad e_n = e_s \times e_\xi \tag{12}$$

with $e_s \equiv e_T$. The ribbon geometry is constructed as an extension of ς in the e_n direction. Hence, it is convenient to parameterize the magnetization in the ribbon as $m = e_s \sin \Theta \cos \Phi + e_\xi \sin \Theta \sin \Phi + e_n \cos \Theta$. Similarly to thin shells,[31,68,98] the energy of the ribbon can be presented in the form

$$E_{rib} = hw \int ds \left(\mathcal{E}_{rib}^x + \mathcal{E}_{rib}^A + \mathcal{E}_{rib}^D \right) \tag{13a}$$

with the energy densities of the exchange and anisotropies[61]

$$\mathcal{E}_{rib}^x = A(\Theta' - \Gamma_1)^2 + A \left[\sin \Theta (\Phi' - \Omega_1) - \cos \Theta \frac{\partial \Gamma_1}{\partial \Phi} \right]^2$$
$$+ A\Gamma_2^2 + A \cos^2 \Theta \left(\frac{\partial \Gamma_2}{\partial \Phi} \right)^2 \tag{13b}$$
$$\mathcal{E}_{rib}^A = -K_1(m \cdot e_s)^2 + K_3(m \cdot e_n)^2$$

Here, the exchange energy and the exchange-induced anisotropy is determined by the effective spin connection $\Omega = \Omega_1 e_s$ with $\Omega_1 = -\kappa \cos \varepsilon$ and vector $\Gamma = \Gamma_1 e_s + \Gamma_2 e_\xi$ with $\Gamma_1 = -\kappa \sin \varepsilon \cos \Phi + (\varepsilon' + \tau) \sin \Phi$ and $\Gamma_2 = (\varepsilon' + \tau) \cos \Phi$. The last term $\mathcal{E}_{rib}^D$ describes the intrinsic DMI. Using the explicit form of the Bloch type DMI[68] and Néel type DMI,[98] one can get the DMI for the ribbon

$$\mathcal{E}_{rib}^{D(B)} = D^{(B)} \sin^2 \Theta \left(2 \sin \Phi \Theta' - \Gamma_1 \sin \Phi + \Gamma_2 \cos \varepsilon \cos \Phi \right)$$
$$\mathcal{E}_{rib}^{D(N)} = D^{(N)} \left(2 \sin^2 \Theta \cos \Phi \Theta' + \kappa \sin \varepsilon \cos^2 \Theta \right) \tag{13c}$$

Here, $D^{(B)}$ and $D^{(N)}$ are the constants of the Bloch type DMI and the Néel type DMI, respectively. The anisotropy stemming from magnetostatics is represented by the coefficients[61,99–101]

$$K_1 = K_1^{mc} + 2\pi M_s^2 N_2, \quad K_3 = K_3^{mc} + 2\pi M_s^2 - 4\pi M_s^2 N_2,$$
$$N_2 = \frac{h}{\pi w} \ln \frac{w}{h} + \frac{3h}{2\pi w} \tag{13d}$$

where the magneto-crystalline anisotropies with the coefficients K_1^{mc} and K_3^{mc} are incorporated. In the case of a magnetically soft ribbon with $K_1^{mc} = K_2^{mc} = 0$, the easy axis is directed along the tangential direction and the easy-plane anisotropy is within the surface ς. In the following, it is convenient to represent Equation (13b) as[61]

$$\mathcal{E}_{eff}^x = A(\Theta' - \tau^* \sin \overline{\Phi})^2 + A \left[\sin \Theta (\overline{\Phi}' + \kappa^*) - \tau^* \cos \Theta \cos \overline{\Phi} \right]^2 \tag{13e}$$

where the effective curvature and torsion are $\kappa^*(s) = \kappa(s) \cos \varepsilon(s) - \upsilon'(s)$ and $\tau^*(s) = \sqrt{\kappa^2(s) \sin^2 \upsilon(s) + [\varepsilon'(s) + \tau(s)]^2}$ with $\tan \upsilon = -\kappa \sin \varepsilon / (\varepsilon' + \tau)$ and angle $\overline{\Phi} = \Phi + \upsilon$. This expression has the form of the exchange energy density of a thin wire (5) with the redefined geometrical parameters.

By comparison of the intrinsic DMI energy of the ribbon with the corresponding energy of the wire, one can conclude that the energy terms for the DMI of Bloch and Néel type in ribbons (13c) can be recovered from the vector expression (7) using $D_T^i = -D^{(B)}$ and $D_N^i = D^{(N)}$, respectively.

The anisotropy energy of a narrow ribbon reads[61]

$$\mathcal{E}_{eff}^A = -K_{eff}^1 \sin^2 \Theta \cos^2 \overline{\Phi} + K_{eff}^3 \cos^2 \Theta \tag{13f}$$

with the effective anisotropy coefficients $K_{eff}^1 = K_1 - A(\varepsilon' + \tau)^2$ and $K_{eff}^3 = K_3 + A(\varepsilon' + \tau)^2$.

To summarize the Section 2, curvilinear wires and ribbons behave as a biaxial chiral helimagnet due to the geometry-induced DMI and anisotropy. This allows to expect phase transitions, which are determined by the strength of the mesoscale DMI (9a) and mesoscale anisotropies (9c) and their mutual spatial orientation. In general, without specifying the geometry

of the object, further quantitative analysis is hardly possible. Therefore, in the following we will consider selected examples: rings, plane curves, and helices with a constant curvature and torsion.

3. Curvilinear Geometry-Induced Effects in Equilibrium Magnetic Textures

3.1. Emergent Geometry-Induced Magnetic Field

In this subsection, we will discuss behavior of systems with a strong anisotropy. This allows us to assume that the magnetic texture, modified by the geometry, will not deviate significantly from the equilibrium state given by the anisotropy. In this case, the geometry-induced anisotropy and DMI act as a source of the emergent geometry-induced magnetic field,[31,60] which influences even the ground state magnetization: an assumed ground state becomes a subject of further modifications due to curvilinear effects.[30–32,60] The concept of the emergent magnetic field provides an intuitive understanding of how the curvilinear geometry influences the magnetic texture. For a sufficiently strong anisotropy K, the resulting ground state should be close to $m = e_T$. However, the strictly tangential magnetization distribution in a curvilinear magnetic wire is impossible. Assuming small deviations from the tangential directions, we utilize the angular parametrization for the magnetization as for the exchange energy expression (5) and put $\Theta = \pi/2 + \vartheta$ with $|\vartheta|, |\Phi| \ll 1$. In this case, the energy density (8) can be presented as follows

$$\mathcal{E} \approx \mathcal{E}_0 + \underbrace{\Phi\left(\tau D_N^i - 2A\kappa'\right) + \vartheta\left(\kappa D_T^i + \tau D_B^i - 2A\kappa\tau\right) + K\left(\vartheta^2 + \Phi^2\right)}_{\mathcal{E}_f} \tag{14}$$

Here, the first term $\mathcal{E}_0$ is the energy density of the strictly tangential distribution and the second term can be presented in the form of the Zeeman-like energy term $\mathcal{E}_f = -M_s F \cdot m$ with the field

$$F = \frac{1}{M_s}\left(2A\kappa' - \tau D_N^i\right)e_N + \frac{1}{M_s}\left(2A\kappa\tau - \kappa D_T^i - \tau D_B^i\right)e_B \tag{15}$$

Previously the concept of the emergent geometry-induced magnetic field was applied for curved wires in the absence of the intrinsic DMI,[60] see also the discussion of the effective geometrical field in magnonic waveguides.[102] Then, the magnetization distribution in the ground state corresponds to the minimum of the energy (14), which results in the magnetization tilting from the tangential distribution $\Theta = \pi/2$ and $\Phi = 0$ by the angles

$$\vartheta \approx \frac{\kappa D_T^i + \tau D_B^i}{2K} - \frac{A}{K}\kappa\tau, \qquad \Phi \approx \frac{A}{K}\kappa' - \frac{D_N^i}{2K}\tau \tag{16}$$

The intrinsic DMI is known to support the magnetization curling, with a tendency to its spiralization. However, even in the absence of the intrinsic DMI, $D^i \equiv 0$, the magnetization angles $\vartheta = \ell^2\kappa\tau$ and $\Phi = \ell^2\kappa'$ are finite for an arbitrary wire. Therefore, the strictly tangential distribution in an intrinsically achiral wire can be realized when $\kappa' = 0$ and $\tau = 0$ only.

3.2. Effects Induced by the Gradient of the Curvature in Plane Wires

We start our discussion from the case of planar wires, where the torsion is absent, $\tau = 0$. Using the angular parametrization for the magnetization as for the exchange energy (5), the minimization of the energy (8) results in the in-plane texture with $\Theta = \pi/2$ and the planar angle Φ, which satisfies the driven pendulum equation[65,95]

$$\Phi'' - \frac{1}{\ell^2}\sin\Phi\cos\Phi = -\kappa' \tag{17}$$

The gradient of the curvature, described by the κ' creates an external stimulus, which can strongly influence the magnetic texture, leading, for example to the driving of noncollinear magnetic textures.

3.2.1. Equilibrium Magnetization Textures in Rings

First, we consider the limiting case of a planar wire with a constant curvature $\kappa = 1/R = \text{const}$, which corresponds to a ring of radius R. In the absence of the intrinsic DMI, the ψ-frame coincides with the TNB reference frame. The magnetization texture is described by Equation (17) without external stimuli since $\kappa' = 0$. Therefore, the equilibrium planar texture satisfies the usual pendulum equation.[60] The solution $\Phi = 0$, π, which is uniform in the local reference frame, corresponds to the planar vortex state with the energy $E_{vor} = 2\pi R S K(\kappa^2\ell^2 - 1)$. The vortex solutions are well known for magnetic nanorings.[103,104] An inhomogeneous solution of the pendulum equation reads[60]

$$\Phi_{on}(\chi) = \frac{\pi}{2} - \text{am}(x,k), \qquad x = \frac{2\kappa s}{\pi}K(k) \tag{18}$$

with $\text{am}(x,k)$ being the Jacobi's amplitude[105] and the modulus k is determined by the condition $2\kappa k K(k) = \pi\ell$. Here, $K(k)$ is the complete elliptic integral of the first kind.[105] This solution with the energy $E_{on} = 2\pi R S K[4\kappa\ell E(k)/(\pi k) - \kappa^2\ell^2 - 1/k^2]$ and $E(k)$ being the complete elliptic integral of the second kind is analogous to the onion state.[103,104] The comparison of the energies of the vortex and onion states gives the critical curvature $\kappa_0 \approx 0.657/\ell$ separating these states.[60] This helimagnet phase transition is qualitatively explained by the relative contribution of the exchange and anisotropy to the total energy of the system. The vortex state appears when the anisotropy dominates and aligns the magnetization along the easy axis. On the other hand, the exchange interaction tends to align $m(s)$ homogeneously in the laboratory reference frame, which is equivalent to the periodic state in the local reference frame. This corresponds to the case of a strong extrinsic DMI.

3.2.2. Equilibrium Magnetization States in a Generic Plane Wire

Now we consider the general case of a planar curved wire, whose geometrical properties are described by the spatially dependent curvature $\kappa(s)$. The ground state of the planar curve
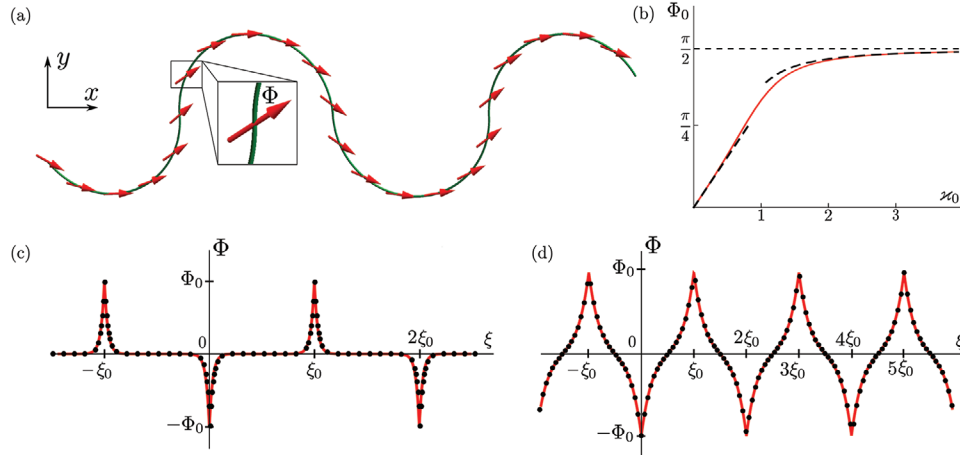
ADVANCED
SCIENCE NEWS
www.advancedsciencenews.com

NANO · MICRO
small
www.small-journal.com

Figure 3. Ground state of the meander shaped wire with periodic curvature. a) Schematics of a ferromagnetic wire (green curve) consisting of half-rings of radius R. The local magnetization direction Φ is indicated with red arrows. b) Maximal tilt angle of the magnetization from the tangential direction Φ_0 (solid line) with asymptotics $\Phi_0 \approx \varkappa_0$ and $\Phi_0 \approx \pi/2[1-1/(4\varkappa_0^2)]$; $\varkappa_0 = \ell/R$. The ground state of the wire with c) $\varkappa_0 = 0.1$ and d) $\varkappa_0 = 0.6$. Solid lines are calculated using Equation (19). Symbols are the results of spin-lattice simulations. Adapted under the terms of the CC BY Creative Commons Attribution 4.0 International License (http://creativecommons.org/licenses/by/4.0/).[66] Copyright 2019, SciPost Foundation.

appears to be also planar with $\Theta = \pi/2$. Its azimuthal angle Φ is described by the driven pendulum equation (17) with the asymptotic solution $\Phi(s) \approx \ell^2 \kappa' + \mathcal{O}(\ell^2 |\kappa'''|/|\kappa'|)$ for the case of small curvatures. In the opposite case of strongly localized δ-shaped curvature $\kappa(s) = \kappa_0 \delta(s)$, which corresponds to a sharp bend of the wire, the ground state magnetization has the form of a planar hook determined by the azimuthal angle $\Phi(s) = -2\,\text{sgn}(s)\arctan e^{(s_0-|s|)/\ell}$ with $s_0 = \ln\tan(\kappa_0/(4\ell))$.[65] For a box-curvature case, which corresponds to the circular arc ending by straight lines without self-intersection, the ground magnetization texture has the form of two hooks in the points of curvature steps with exponential tails.[65] A meander shaped wire has a periodically changing curvature, which leads to periodic hooks in the magnetization distribution[66]

$$\Phi(s) = (-1)^\lambda \,\text{am}\left(\frac{s - \pi R(\lambda + 1/2)}{k\ell}, ik\right),$$
$$\lambda = \left\lfloor \frac{s}{\pi R} \right\rfloor, \quad k = \frac{R}{\sqrt{\ell^2 - R^2 \sin^2 \Phi_0}} \tag{19}$$

where $\lfloor \bullet \rfloor$ is the floor operator, R is the ring radius and the value Φ_0 is determined via the elliptic integral of the first kind $F(\Phi_0, ik) = \pi R/(2\ell k)$, see **Figure 3**.

The driven pendulum (17) implies that the ground state cannot be homogeneous in the local reference frame if the curvature $\kappa \neq$ const. The latter also leads to the geometry-induced motion of magnetic domain walls.[106]

3.2.3. Domain Walls in Curved Plane Wires: Curvature-Induced Pinning

Domain walls are among the simplest nonlinear excitations in magnetic systems. Ferromagnetic wires with the easy-axis anisotropy along the tangential direction support transverse domain walls. Here, we consider the impact of a

spatially-dependent curvature on this texture. To describe the domain wall in a planar curved wire, it is instructive to exploit the angular parametrization (6). Then, similar to Equation (17), the equilibrium magnetization textures are necessarily to be planar with $\phi = \phi_0 = 0$, π with θ being determined by a driven pendulum equation[95]

$$\theta'' - \frac{1}{\ell^2}\sin\theta\cos\theta = -\kappa'\cos\phi_0 \tag{20}$$

It is known that the free pendulum equation has a kink solution $\cos\theta = \pm\tanh(s/\Delta)$, which corresponds to the domain wall in a rectilinear or circular wire, when $\kappa' = 0$. The coordinate-dependent curvature becomes a source of the additional driving force responsible for the curvature-induced domain wall dynamics. To analyze the domain wall static and dynamic properties, we restrict our consideration to $\ell^2 \kappa' \ll 1$, which allows to use a collective variable approach based on a q-Φ model[107–109]

$$\cos\theta = -p\tanh\left[\frac{s - q(t)}{\Delta}\right], \qquad \phi = \Phi(t) \tag{21}$$

where p is the polarity that defines the type of the domain wall (e.g., $p = +1$ for head-to-head and $p = -1$ for tail-to-tail type), q is the domain wall position, Δ is the domain wall width. The phase Φ determines the orientation of the transversal magnetization component inside the wall, being canonically conjugated variable to q. In the limit of a narrow domain wall, $\kappa\Delta \ll 1$, the total micromagnetic energy (8) of the domain wall reads[95]

$$E^{\text{DW}} = \frac{\mathcal{S}K}{2\pi M_s^2}\left[\frac{\ell^2}{\Delta} + \Delta + \pi p\ell^2\kappa(q)\cos\Phi - \ell^2\Delta\kappa^2(q)\sin^2\Phi\right] \tag{22}$$

where $\mathcal{S}$ is the area of the wire cross-section. The first and second terms in Equation (22) represent the competition between the exchange and anisotropy energies, that defines the domain wall width in the rectilinear wire, $\Delta \approx \ell$. The third and last terms in
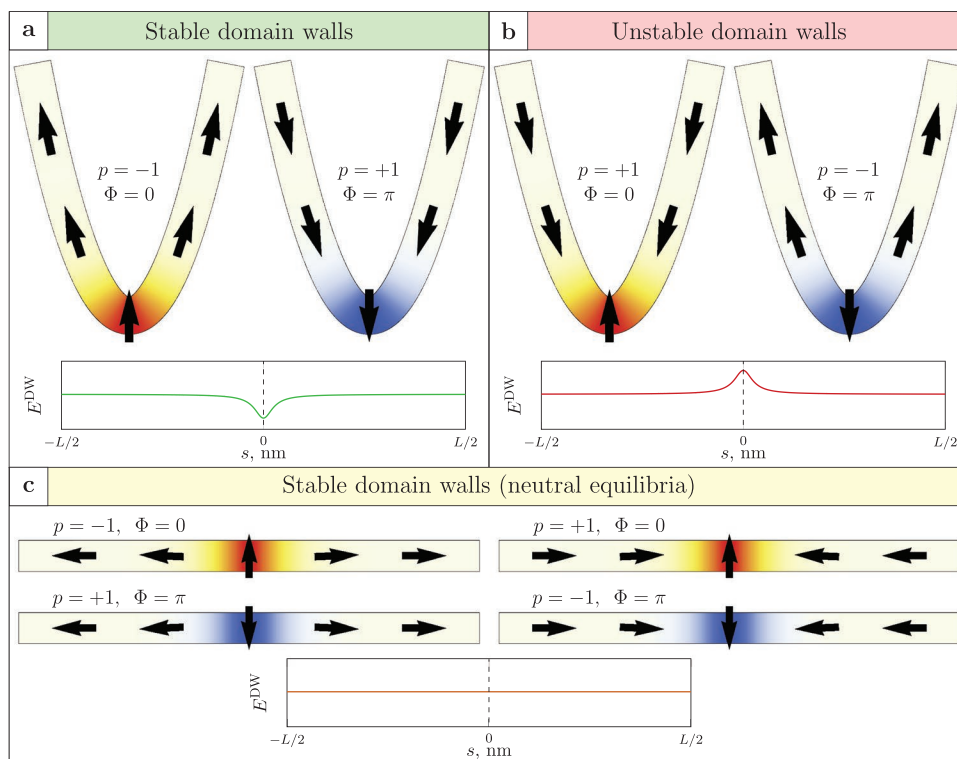
Figure 4. Chiral symmetry breaking in magnetic parabolas. a) Stable tail-to-tail and head-to-head domain walls and the energy landscape at the domain wall position along the parabolic stripe. The energy landscape is calculated by means of the q-Φ model. The potential well at the apex region appears due to the influence of the curvature–induced DMI. b) Unstable head-to-head and tail-to-tail domain walls and the corresponding energy landscape with the potential wall at the apex region. c) Transversal domain walls in a straight stripe. All walls are energetically same and in the neutral equilibrium within the framework of the q-Φ model. Adapted with permission.[42] Copyright 2019, American Physical Society.

Equation (22) originate from the DMI and anisotropy terms, respectively, which appear in the exchange energy due to curvature. The minimization of Equation (22) with respect to parameters q and Φ results in the equilibrium values q_0 and Φ_0

$$\kappa'(q_0) = 0, \quad \cos\Phi_0 = -p \tag{23}$$

Thus, the domain wall is pinned at the local extremum of the curvature distribution, while the domain wall phase is selectively defined by the polarity p. This phase selection is an illustrative example of the geometry-induced chirality breaking:[30,36] the curvature-induced DMI selects the handedness even for achiral textures, providing the phase-selective pinning of domain walls.

To illustrate the influence of the curvature gradients on domain walls, it is insightful to consider a parabolic wire, which is mathematically the simplest curve with well-defined geometrical properties and $\kappa(\pm\infty) = 0$. In this case, the resulting energy of the head-to-head and tail-to-tail types of domain walls with different polarities contains the asymmetry, which originates from the exchange-induced DMI in curvilinear systems: the tail-to-tail and head-to-head domain walls with polarities $p = -1$ and $p = +1$, respectively, feel the potential well at the apex region of the parabolic stripe, see **Figure 4**a, while the same types of domain walls with opposite polarities are unstable due to the potential wall in the curvilinear region,

see Figure 4b. This finding is in contrast to the case of infinitely long straight wires, that provide the neutral equilibrium for all types of domain walls and their polarities, Figure 4c.

Although these effects stemming from the exchange interaction in curvilinear wires are generic, it is difficult to find them in experiments as they might be hidden by other magnetic interactions like the long-range magnetostatic interaction. The very first experimental confirmation of the existence of exchange-induced chiral interactions was provided in parabolic nanostripes made of permalloy.[42] The discussed above theoretical prediction was studied by means of X-ray magnetic circular dichroism photo electron emission microscopy (XMCD-PEEM) during the magnetization reversal of plane parabolic stripes. The resulting hysteresis loops revealed the presence of a specific two-step switching process with three easily identifiable plateaus, that referred to stable magnetic states: tail-to-tail ($p = -1$) and head-to-head ($p = +1$) domain walls and the quasi-tangential magnetic state along the parabolic stripe.[110] At the first switching event, a stable tail-to-tail domain wall, pinned by the curvature–induced exchange-driven DMI, was expelled, which led to the transition to the quasi-tangential magnetization state along the parabolic stripe. At the second switching event, a stable head-to-head domain wall nucleated from the end of a parabolic branch and propagated into the apex area. By analyzing these experimental results with full-scale micromagnetic simulations and analytical calculations, it was

ADVANCED
SCIENCE NEWS

www.advancedsciencenews.com

NANO · MICRO

small

www.small-journal.com

possible to quantify the strength of the exchange-induced DMI constant, $D^x = 2A\kappa$, see Equation (4), from the first switching field B^{DMI}[42]

$$D^x = B^D \sqrt{\frac{Aw}{2h[2\ln(w/h)+3]}} \qquad (24)$$

with w and h being the stripe width and thickness, respectively and A being the exchange constant. The resulting value D^x was found to be comparable to the surface-induced DMI obtained for asymmetric Co sandwiches.[111] Furthermore, its value can be tuned by changing the local curvature at the apex region of the parabola.

3.3. Effects Induced by the Torsion in Wires and Ribbons

A nonzero torsion τ in a wire breaks the geometrical chiral symmetry that is directly transferred to the magnetization distribution.[62] We start the description of the torsion-induced effects using a helix wire: a remarkable feature of this 3D geometry is that its curvature and torsion are coordinate independent. Therefore, all effects related to the interplay between the geometry of the system and the geometry of the magnetic texture can be analyzed in this system in the most straightforward and intuitively understandable way.[64] A magnetic helix is one of the simplest geometries to address the geometry-induced chirality breaking, where the geometry-induced chiral DMI can enable an interplay between the geometrical chirality of the wire and the magnetochirality of the magnetic texture.

3.3.1. Curvature and Torsion Effects: Helix Wire as a Case Study

Helices of a constant radius R and pitch P is a prototypical magnetic 1D system immersed in 3D space allowing to highlight all curvature and torsion effects in magnetic wires, see Figure 2a. Using the arc-length parametrization, a helix can be represented as

$$\gamma(s) = \hat{x}R\cos\frac{s}{s_0} + \hat{y}R\sin\frac{s}{s_0} + \hat{z}\frac{\mathcal{C}Ps}{2\pi s_0} \qquad (25)$$

where $\mathcal{C} = \pm 1$ is the helix chirality (left and right helices) and $s_0 = \sqrt{R^2 + P^2/(2\pi)^2}$. The torsion and curvature read as $\tau = \mathcal{C}P/(2\pi s_0^2)$ and $\kappa = R/s_0^2$, respectively. Alternatively, radius and pitch read $R = \kappa/(\kappa^2 + \tau^2)$ and $P = 2\pi\tau/(\kappa^2 + \tau^2)$, respectively. The mesoscale DMI results in the appearance of the quasi-tangential and periodic magnetization states in the local reference frame. In the following, we will consider $D^i = -D^i e_T$ as a case study with the critical value of DMI $D_c^i = 2\sqrt{AK}$.

To identify the physical origin of the magnetic responses of a helical wire, it is convenient to align the reference frame with the principal axes of the anisotropy (ψ-frame). Then the energy density reads[64,93]

$$\mathcal{E} = Am'_\alpha m'_\alpha - \mathcal{K}_1 m_1^2 + \mathcal{K}_2 m_2^2 + \varepsilon_{\alpha\beta\gamma}D_\alpha m_\beta m'_\gamma \qquad (26)$$

The rotation of the reference frame is applied around the normal direction e_N. In the limiting case of small curvatures $\kappa\ell \ll 1$ and $|\tau_{eff}|\ell \ll 1$, the rotation angle[62,93]

$$\psi \approx \ell^2\kappa\tau_{eff}, \qquad \tau_{eff} = \tau - \frac{D^i}{\ell D_c^i} \qquad (27a)$$

The biaxial anisotropy in Equation (26) is determined by the coefficients of the easy-axis anisotropy $\mathcal{K}_1 \approx K + A(\tau_{eff}^2 - \kappa^2)$ and the easy-plane anisotropy $\mathcal{K}_2 \approx A\kappa^2$. As a mutual effect of the intrinsic anisotropy K and curvature-induced anisotropy, the easy-axis direction e_1 becomes tilted from e_T by the angle ψ in the rectifying plane. Hence, the ground state magnetization of the quasi-tangential state (homogeneous in the local reference frame), parameterized as for the exchange energy expression (5), is determined by the equilibrium angles

$$\Theta_t = \frac{\pi}{2} - \psi, \qquad \cos\Phi_t = \mathfrak{C} = \pm 1 \qquad (27b)$$

The in-plane anisotropy has the hard axis $e_2 = e_N$. Thus, the ground state of the helix wire with the easy-axial anisotropy along the tangential direction is described by $m = e_1$. This quasi-tangential state is tilted by the angle (27a) from the assumed easy-axial state along e_T. Qualitatively, this tilt is described by the concept of the emergent magnetic field, see Equation (16). The binormal component of the magnetization of the tilted state is determined by the product of the helix chirality $\mathcal{C}$ and the magnetochirality of the texture $\mathfrak{C}$,[62] see Figure 2a. This coupling between the geometrical and magnetic chiralities is the manifestation of the geometry-induced chirality breaking. In a general case, the directions e_1 and e_2 are determined by both, the exchange-driven and intrinsic DMI with $e_2 \neq e_N$. The mesoscale DMI in Equation (26) is represented by the vector $D \approx 2A(\tau_{eff}e_1 + \kappa e_3)$, confer, Equation (9b). We can compare the strength of the intrinsic and extrinsic DMI. For a helix wire, $D_1^x \approx 2A\tau = 4\pi AP/(P^2 + 4\pi^2R^2)$. Using typical values $A = 10$ pJ m^{-1}, we obtain that $D_1^x = 0.14$ mJ m^{-2} for a helix with the radius $R = 50$ nm and the pitch $P = 300$ nm; $D_1^x = 0.07$ mJ m^{-2} for $R = 100$ nm, $P = 600$ nm. These values are comparable to those estimated by the ab initio calculations for multilayer systems.[112,113]

3.3.2. Helimagnetic Phase Transition

A strong mesoscale DMI (9b) can result in the phase transition from the quasi-tangential to a periodic state, whose texture is determined by the orientation of D with respect to the anisotropy axes. The elliptical helicoid state is the most general case of the periodic state in a helix, with a modulation of the magnetization around the given D direction. Also, by tuning the ratio between the intrinsic and extrinsic DMI for the case $D_N^i = 0$, it is possible to recover two periodic states, characteristic for a straight wire: i) the cycloidal state appears in the case of $D \cdot e_1 = 0$ with the chiral modulation of the magnetization around e_3, and ii) the helicoidal state appears in the case of $D \cdot e_3 = 0$ with the chiral modulation of the magnetization around e_1, see Figure 2c.[93]

**ADVANCED
SCIENCE NEWS**

www.advancedsciencenews.com

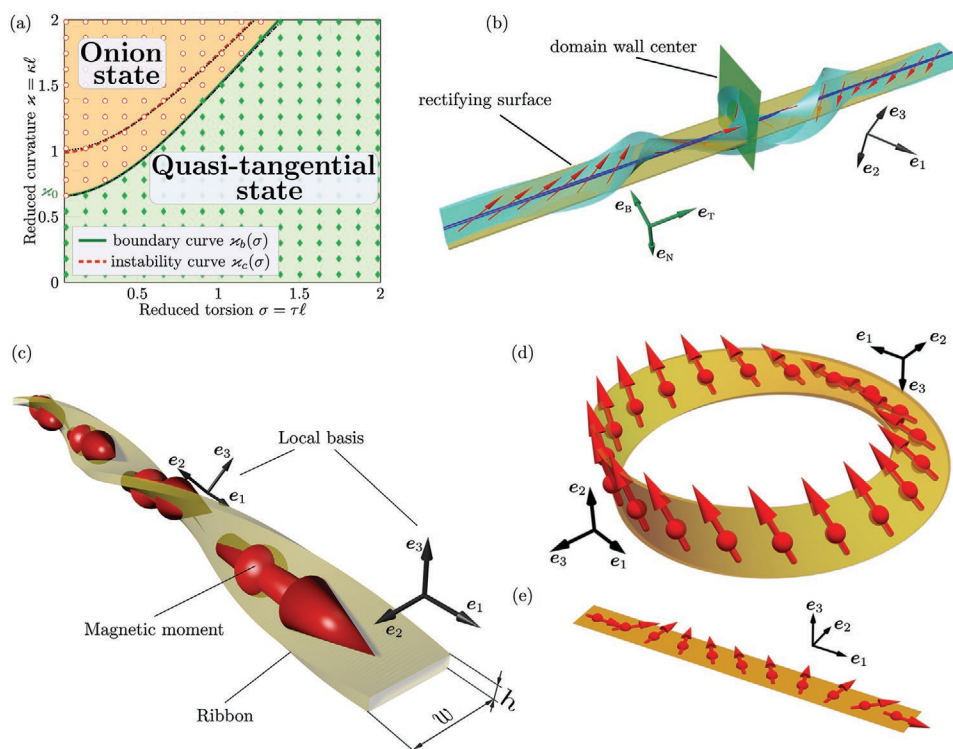NANO · MICRO
small

www.small-journal.com

Figure 5. Effects of curvature and torsion on static magnetic textures. a) Helimagnetic phase transition between the onion and quasi-tangential states in helix wires. Reproduced with permission.[62] Copyright 2015, American Physical Society. b) Schematics of the untwisted domain wall in a helix wire with $\tau > 0$. The magnetization direction, TNB and ψ reference frames are shown by red, green, and black arrows, respectively. Adapted under the terms of the CC BY Creative Commons Attribution 4.0 International License (http://creativecommons.org/licenses/by/4.0/).[64] Copyright 2016, Springer Nature. c) Straight narrow ribbon with torsion $\tau > 0$. For this object, the central curve p is a straight line. This magnetic texture resembles one of a straight wire with zero curvature and non-zero torsion. Reproduced with permission.[61] Copyright 2017, IOP Publishing. All rights reserved. d) Möbius ribbon in the so-called magnetic "ribbon state." For this object, the central curve γ is a ring. This magnetic texture corresponds to one of a closed curve of constant curvature and nonzero torsion. Reproduced with permission.[61] Copyright 2017, IOP Publishing. All rights reserved. e) Untwisted Möbius ribbon shown in (d). Reproduced with permission.[61] Copyright 2017, IOP Publishing.

The periodic equilibrium state in a helix wire is analogous to the onion state in a ring and its magnetization texture reads[93]

$$\theta_{\mathrm{per}} = \frac{\pi}{2} + \theta_{\mathrm{per}}^0(\chi), \qquad \phi_{\mathrm{per}} = -\chi + \phi_{\mathrm{per}}^0(\chi) \tag{28}$$

with $\chi = -Ds/(D_c^i \ell)$, and $\theta_{\mathrm{per}}^0(\chi)$ and $\phi_{\mathrm{per}}^0(\chi)$ being 2π-periodic functions. Note, that in the case of $D^i = 0$, the period of this state matches with the geometrical period of the helix.[62]

The character of the transition between the quasi-tangential and periodic states is governed by the strength of the intrinsic DMI.[93] If $D_T^i = D_c^i$, the quasi-tangential state is impossible for any torsion and curvature. Otherwise, the quasi-tangential state can be stabilized in a certain region of the $(\tau_{\mathrm{eff}}, \kappa)$ phase diagram, see **Figure 5**a plotted for the case of $D_T^i = 0$. A finite size of the helix leads to the transition between the periodic and quasi-tangential states thought the so-called periodic domain walls state. The boundary between the periodic and quasi-tangential states can be fitted as

$$\kappa_{\mathrm{b}} \approx \sqrt{C_1 + C_2 \tau_{\mathrm{eff}}^2} \tag{29}$$

with $C_1 \approx \kappa_c^2$ and $C_2 = 2$ in the case of absence of intrinsic DMI.[62]

3.3.3. Torsion Effects on Domain Walls

While domain walls in planar curved wires are described by the q-Φ model (21), a nonzero torsion typically causes the rotation of the phase of the domain wall. The reason for this effect is the extrinsic DMI, which contains the wire torsion, see Equation (4). We note that the intrinsic DMI favors the spiralization of the magnetization texture. In particular, the phase rotation of the domain wall is known to occur in biaxial stripes with the intrinsic DMI.[114] Generalizing the q-Φ model (21) by taking into account a possible phase rotation, the domain wall structure in a helical wire can be described by the following ansatz[64]

$$\cos\theta = -p \tanh\frac{s-q}{\Delta}, \quad \phi = \Phi - Y(s-q) \tag{30}$$

For a uniaxial chiral magnet with the DMI structure equivalent to the case $\boldsymbol{D} \parallel \boldsymbol{e}_1$, there is the exact solution with $\Delta = A/\sqrt{\mathcal{K}_1 - D_1^2/4}$ and $Y = D_1/(2A)$. The domain wall structure

**ADVANCED
SCIENCE NEWS**
www.advancedsciencenews.com

**NANO · MICRO
small**
www.small-journal.com

in such a curvilinear wire can be determined by the variational approach using the domain wall width Δ and its slope Y in Equation (30) as variational parameters. The integration of the energy density (26) with D lying in the TB plane gives[64]

$$\frac{E}{\mathcal{S}} = \underbrace{A\left(\frac{2}{\Delta} + 2\Delta Y^2\right)}_{\text{exchange}} + \underbrace{2\Delta\mathcal{K}_1 + \Delta\mathcal{K}_2\left(1 + \mathcal{C}_1\cos 2\Phi\right)}_{\text{anisotropy}}$$
$$+ \underbrace{p\mathcal{C}_2 D_3\cos\Phi - 2\Delta D_1 Y}_{\text{DMI}}, \tag{31}$$
$$\mathcal{C}_1 = \frac{\pi\Delta Y}{\sinh(\pi\Delta Y)}, \qquad \mathcal{C}_2 = \frac{\pi(1 + \Delta^2 Y^2)}{\cosh(\pi\Delta Y/2)}$$

In the case of small curvatures and torsions, the equilibrium domain wall parameters are[64]

$$Y \approx \frac{D_1}{2A} \qquad \text{and} \qquad \Delta \approx \ell \tag{32}$$

see Figure 5b. Thus, the first component of the mesoscale DMI D_1 acts on the slope of the azimuthal angle ϕ of the magnetization within the DW, while the second component D_3 breaks the symmetry of the domain wall with respect to the opposite topological charges p with the equilibrium phase $\Phi = (1+p)\pi/2$. In the absence of the intrinsic DMI, the equilibrium magnetochirality $\mathfrak{C} = -\text{sgn}\,Y = -\text{sgn}\,\tau$, that is, it is opposite to the geometrical chirality of the helix. This coupling between geometrical and magnetic chiralities illustrates the geometry-induced chirality breaking.

3.3.4. Narrow Helicoid Ribbon as a Straight Wire with Torsion

We apply the developed micromagnetic framework for magnetic ribbons to analyze narrow helicoid ribbons. For this geometry, the central curve is a straight line $\gamma(s) = s\boldsymbol{e}_z$. The helicoid is characterized by the constant rate of turning about γ, hence the orientation of the line segment turning $\Psi(s) = \mathcal{C}s/(\overline{s}\ell)$, where $\overline{s}$ determines the helicoid period in units of the magnetic length. The peculiarity of a narrow helicoid ribbon is in its magnetic properties, which can be described by effective straight magnetic wire, $\kappa^* = 0$, with the effective torsion $\tau^* = 1/(\overline{s}\ell)$,[61] see Figure 5c. For the case of a magnetically soft helicoid ribbon, we obtain in-surface ground state magnetization with $\Theta = \pi/2$ and $\cos\Phi = \cos\overline{\Phi} = \mathfrak{C}$, and magnetochirality $\mathfrak{C} = \pm 1$. We note that accounting for magnetoelastic interactions and the intrinsic DMI lead to the geometrical transitions between helicoid, DNA-like and cylindrical states in the ribbon.[68] The helimagnetic phase transition is absent for this system within the narrow ribbon assumption (10) because the mesoscale DMI vector is parallel to the magnetization. At the same time it influences the spin wave spectrum, see Section 4.

3.3.5. Narrow Möbius Ribbon as a Circular Wire with Torsion

A narrow Möbius ribbon micromagnetically behaves as a planar circular wire with torsion.[61] The central line of the Möbius ribbon is a circle $\gamma(\chi) = R[\boldsymbol{e}_x\cos\chi + \boldsymbol{e}_y\sin\chi]$,

while the rate of turning around γ is determined by $\Psi(\chi) = \pi - \mathcal{C}\chi/2$. Finally, the micromagnetic properties of such a ribbon correspond to a 1D wire with the effective curvature $\kappa^* = -2\cos(\chi/2)[1 + 2\sin^2(\chi/2)]/[1 + 4\sin^2(\chi/2)]$ and torsion $\tau^* = -\mathcal{C}\sqrt{1 + 4\sin^2(\chi/2)}/(2R)$ possessing antiperiodic boundary conditions,[61] see Figure 5d,e. The coefficient of the effective easy-axis anisotropy $K_1 \propto R^2$, which leads to the realization of the vortex state for a large ribbon radius. An inhomogeneous ribbon state appears for small radii (small effective anisotropy).[61] In contrast to the planar onion state in ferromagnetic rings, the geometry-induced anisotropy prevents the magnetization to be within the xy plane. We note that Möbius ribbons possess a topologically protected domain wall as a ground state if the anisotropy with the easy axis along $\boldsymbol{e}_N$ exceeds a critical value, otherwise the vortex state is realized.[115,116] The torsion of the ribbon results in the chiral symmetry breaking: the magnetochirality of the domain walls in Möbius rings becomes determined by the geometrical chirality of the ring.[116]

4. Magnetization Dynamics in Curvilinear Wires

Previously, we have discussed the static effects caused by the geometry-induced interactions: emergent biaxial anisotropy and emergent DMI. In dynamics, there appear novel manifestations of these emergent interactions. In particular, it is known that the emergent biaxial anisotropy becomes the source of the Walker limit of the current-induced dynamics of domain walls in uniaxial circular-shaped wires.[63] Another prominent example in magnetization dynamics is the pattern-induced chirality breaking,[30,36] where the chiral symmetry breaking occurs dynamically on the background of a chiral-degenerated static magnetization texture. To discuss the dynamical effects, we consider the temporal evolution of the magnetization vector $\boldsymbol{m}$, based on the Landau–Lifshitz–Gilbert equation

$$\dot{\boldsymbol{m}} = \frac{\gamma_0}{M_s}\boldsymbol{m}\times\frac{\delta E}{\delta\boldsymbol{m}} + \alpha\boldsymbol{m}\times\dot{\boldsymbol{m}} + \boldsymbol{T} \tag{33}$$

where dot means derivative with respect to time t, $\gamma_0 > 0$ is the gyromagnetic ratio, α is the Gilbert damping and $\boldsymbol{T}$ is an additional torque related to spin current in the system.

In the following, we discuss dynamic features of two different types of excitations of the magnetic texture. We start with the consideration of linear dynamics, which is the dynamics of spin waves in curvilinear wires and ribbons. The theoretical framework of magnon dynamics in curved magnets in an important step in the development of the curvilinear magnonics. Among other effects, we will discuss the physical consequences of bending and twisting of magnetic wires, which result in bounding of spin waves by local bends and the nonreciprocity of spin waves due to the wire twisting. Then, we continue with the analysis of the dynamics of topologically protected magnetic states (domain walls), which is another prospective direction of curvilinear magnetism.[30,34] We will discuss how curvature can induce the dynamics of domain walls.

4.1. Geometry-Induced Effects in Spin Wave Dynamics: The Onset of Curvilinear Magnonics

Curvilinear magnonics is part of the rapidly developing research field of 3D magnonics.[117–121] It relies on the use of 3D objects and offers the possibility to develop novel concepts, phenomena, devices and techniques as outlined in the 2021 Magnonics Roadmap.[122] Recently, curvilinear magnetism of nanowires and narribbons put forth a number of concepts for applications in curvilinear magnonics.[30] This includes spin-wave transport in a micro-waveguide,[123] curvature–induced magnonic crystals,[66] magnonic waveguides with the designed band gap spectrum,[102,124] filtering of magnon spectrum based on bounding of spin waves by local bending of magnetic wire,[65] spin waves propagation over a distance ten times larger in a corrugated waveguide than in planar waveguides,[125] magnonic logic elements based on the nonreciprocity of the spin-wave spectrum in ferromagnet helix wires,[62] geometrically tunable magnon spectrum in antiferromagnetic nanohelices.[86] Here, we review the theoretical framework of spin wave description in curvilinear nanowires.

4.1.1. Curvature-Induced Localization of Magnon Modes

We base our description on the phenomenological Landau–Lifshitz–Gilbert equation (33). Using the angular parametrization for magnetization for the exchange energy expression (5) of the magnetization unit vector m, we describe the linear magnetization dynamics by means of a complex-valued function $\Psi = \vartheta + i\varphi$ constructed from the deviations from the equilibrium state: $\Theta(s, t) = \Theta_0(s) + \vartheta(s, t)$ and $\Phi(s, t) = \Phi_0(s) + \varphi(s, t)/\sin\Theta_0(s)$. Without damping, the linear dynamics of the magnetization in the vicinity of the equilibrium state, described by $\Theta_0(s)$ and $\Phi_0(s)$ has the form of the generalized Schrödinger equation[62,126]

$$-\frac{i}{\omega_0}\dot{\Psi} = \hat{H}\Psi + W\Psi^*, \quad \hat{H} = \left(-i\ell\,\partial_s - \mathcal{A}\right)^2 + 1 + V \tag{34}$$

where the overdot denotes the time derivative and $\omega_0 = 2K\gamma_0/M_s$ is the frequency of the uniform ferromagnetic resonance for a straight wire.

In the general case of a 3D wire with the coordinate-dependent curvature and torsion, the effective potentials read

$$V = \frac{3}{4}\left(\cos^2\Theta_0\cos^2\Phi_0 - 2\sin^2\Phi_0\right) + \frac{\ell^2}{2}\left[\sin^2\Theta_0\left(\Phi_0' + \kappa\right)^2 + \Theta_0'^2\right]$$
$$+ \frac{\ell^2\tau^2}{8}\left(2\sin^2\Theta_0\cos 2\Phi_0 - \cos 2\Theta_0 - 3\right) \tag{35a}$$
$$+ \ell^2\tau\left[\sin\Theta_0\cos\Theta_0\cos\Phi_0\left(\Phi_0' + \kappa\right) + \sin\Phi_0\Theta_0'\right]$$

$$W = \frac{1}{2}\left(\sin\Phi_0 + i\cos\Theta_0\cos\Phi_0\right)^2$$
$$- \frac{\ell^2}{2}\left[\sin\Theta_0\left(\Phi_0' + \kappa\right) - i\Theta_0' + \tau\left(\cos\Theta_0\cos\Phi_0 - i\sin\Phi_0\right)\right]^2 \tag{35b}$$

$$\mathcal{A} = -\ell\tau\sin\Theta_0\cos\Phi_0 - \ell\cos\Theta_0\left(\Phi_0' + \kappa\right) \tag{35c}$$

We note that spin waves in a straight wire are described by the standard Schrödinger equation for the complex magnon wave function Ψ with a typical potential scattering. The curvature induces additional geometrical potential, which results in the modification of the scalar potential V, see Equation (35a): the picture is similar to the dynamics of quantum-mechanical particles constrained to a curved wire.[94] Besides, there appears a curvature-induced coupling potential W, see Equation (35b), and the corresponding eigenvalue problem becomes different from the usual set of coupled Schrödinger equations, see discussion in ref. [126]. Such a problem can be treated by applying the Bogoliubov transformation $\Psi = u(s)e^{i\omega t} + v^*(s)e^{-i\omega t}$. Then the problem of the magnon spectrum analysis is converted to the eigenvalue problem $\mathbb{H}|\Psi\rangle = (\omega/\omega_0)|\Psi\rangle$ for the Bogoliubov-de Gennes Hamiltonian $\mathbb{H} = \left\|\begin{matrix} H & W \\ -W & -H \end{matrix}\right\|$, where $|\Psi\rangle = \left\|\begin{matrix} u \\ v \end{matrix}\right\|$.[66] Both the scalar potential V and the coupling potential W are caused by the deviation of the magnetization from the tangential direction. They are present even for a curvilinear planar wire with $\cos\Theta_0 = 0$[62]

$$V = -\frac{1}{2}\left[3\sin^2\Phi_0 + \ell^2\left(\Phi_0' + \kappa\right)^2\right], \quad W = \frac{1}{2}\left[\sin^2\Phi_0 - \ell^2\left(\Phi_0' + \kappa\right)^2\right] \tag{36}$$

The third effective potential is described by $\mathcal{A}$, see Equation (35c). One can see from the Hamiltonian (34) that it acts in the same way as the vector-potential $\boldsymbol{\mathcal{A}} = \mathcal{A}e_\mathrm{T}$ acts in the Hamiltonian of a charged particle. Therefore, one can interpret the quantity

$$\boldsymbol{\mathcal{B}} = \nabla\times\boldsymbol{\mathcal{A}} = \kappa\mathcal{A}e_\mathrm{B} \tag{37}$$

as an effective magnetic flux density. It is supported by the effective current, generated by the magnetic texture in a curved wire, $\nabla\times\boldsymbol{\mathcal{B}} = 4\pi\boldsymbol{j} = -e_\mathrm{N}[\kappa\tau\mathcal{A} + (\kappa\mathcal{A})']$. The appearance of the effective magnetic field, characterized by the vector potential $\mathcal{A}$, breaks the symmetry of the spin-wave spectrum with respect to the direction of the spin-wave propagation. We will see below that it can result in the nonreciprocal radiation of spin waves.

To illustrate this general approach, we will consider several examples. As the simplest case, a plane ring-shaped wire possesses standing waves with the frequency, determined by the curvature. The magnon spectrum on the background of the vortex state can be found using the partial wave expansion[62]

$$\omega = \omega_0\sqrt{\left(1 + \kappa^2\ell^2 m^2\right)^2 - \kappa^4\ell^4} \tag{38}$$

with $m \in \mathbb{Z}_+$ being the azimuthal quantum number. By comparing with the dispersion law of a straight wire, $\omega = \omega_0\sqrt{1 + k^2\ell^2}$ with $k = \kappa m$ being the corresponding wave vector, we see that the curvature decreases the gap in the spin wave spectrum.

An inhomogeneous spatial distribution of the curvature can drastically change the physical picture: even for the case of a plane wire, the inhomogeneous texture of the ground state produces effective potentials (36). These potentials can bound magnon states, providing truly local modes. In particular, the wire with a half-circumference arc (a shallow box curvature)
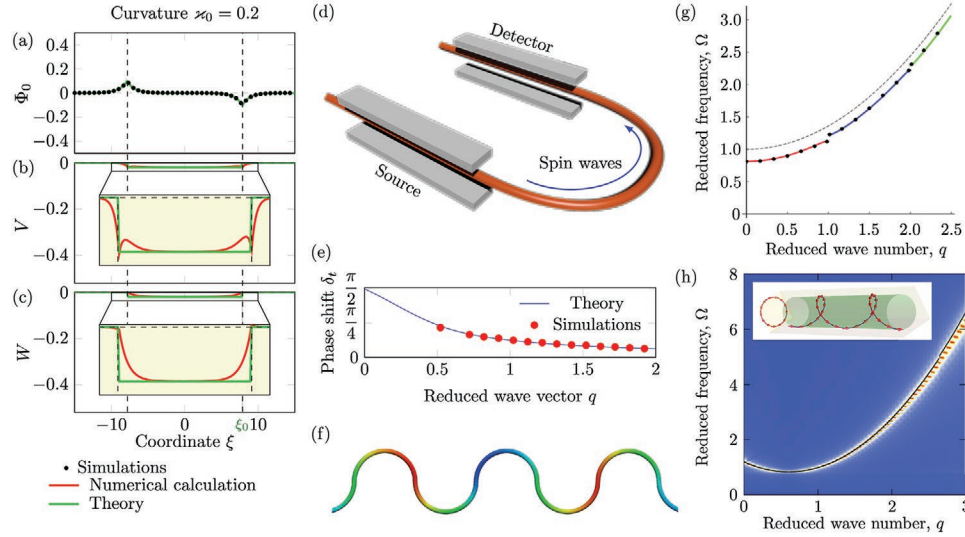
ADVANCED
SCIENCE NEWS
www.advancedsciencenews.com

NANO · MICRO
small
www.small-journal.com

Figure 6. Spin waves in curvilinear wires. a) The magnetic ground state of the wire with a single circular bend (curvature $\kappa_0 = 0.2/\ell$) and respective b,c) spin-wave potentials (36). Reproduced with permission.[65] Copyright 2018, AIP Publishing. d) The concept of a curvilinear spin-wave transmitter with a single mode (40) localized at the circular bend. e) The phase shift of the transmitted spin wave. Adapted with permission.[65] f) Periodically bent wire as a magnonic crystal. The change of the out-of-plane magnetization is indicated with color. Adapted under the terms of the CC BY Creative Commons Attribution 4.0 International License (http://creativecommons.org/licenses/by/4.0/).[66] Copyright 2019, SciPost Foundation. g) The band spectrum of spin waves for $\kappa_0 \ell = 0.6$, calculated using numerical solutions (solid lines) and spin-lattice simulations (symbols). Adapted under the terms of the CC BY Creative Commons Attribution 4.0 International License (http://creativecommons.org/licenses/by/4.0/).[66] Copyright 2019, SciPost Foundation. h) A dispersion relation for spin waves in the helix wire ($\kappa\ell = 0.5$, $\tau\ell = 0.5$) with the easy-tangential anisotropy. Reproduced with permission.[62] Copyright 2015, American Physical Society.

supports the local mode with a frequency $\omega = \omega_0[1 - \pi^2\ell^2/(16R^2)]$ with $R \gg \ell$ being the radius of the arc bending.[65] In the opposite case of a sharp bend of wires with the opening angle α_0, the curvature has δ-like behavior, $\kappa(s) = (\pi - \alpha_0)\delta(s)$. The corresponding eigenfrequency strongly depends on the bend sharpness $\zeta = (\pi - \alpha_0)/2$[65]

$$\omega_{loc} = \frac{\omega_0}{2}\cos\zeta\left(\cos\zeta + \sqrt{1 + 3\sin^2\zeta}\right) \qquad (39)$$

The analysis can be performed also for the general case of a planar curved wire with a coordinate-dependent weak curvature $\kappa(s) \ll 1/\ell$. This case corresponds to the quantum-mechanical problem of a quantum particle in a shallow well, providing the frequency of bound magnons[65]

$$\omega_{loc} = \omega_0\left\{1 - \frac{\ell^2}{16}\left[\int_{-\infty}^{\infty}\kappa^2(s)ds\right]^2\right\} \qquad (40)$$

see **Figure 6**d,e. The interaction of the local mode with spin waves, propagating through the bend, results in the shift of the wave phase according to the Levinson theorem, see Figure 6e.

4.1.2. Curvature-Induced Magnonic Crystals

Another intriguing feature of the magnon spectrum of curvilinear magnetic wires appears when the wire shape is periodically deformed. The periodically varying curvature generates

inhomogeneous equilibrium magnetization texture, which is also periodic. Then the spin wave dynamics is described by the generalized Schrödinger Equation (34) with periodic potentials (35). The periodic potential in quantum-mechanics is known to result in the appearance of a band structure. Similar arguments can be applied for Equation (34).[66] This idea is illustrated with a meander shaped wire, see Figure 6f: the periodic spatial modulation of the ground state (19) results in the band structure for magnons. Extending the two-component approximation[127] for the case of the generalized Schrödinger equation, the band gap edges read[66]

$$\omega_\nu^{\pm} \approx \omega_0\sqrt{\left(1 + \nu^2\ell^2\kappa_0^2 + V_0 \mp V_\nu\right)^2 - \left(W_0 \mp W_\nu\right)^2}, \quad \nu \in \mathbb{N} \qquad (41)$$

see Figure 6g with V_i, W_i, $i \in \mathbb{Z}_+$ being the Fourier components of the potentials V and W, respectively. For a small curvature, $\max|\kappa| = \kappa_0 \ll 1/\ell$, all band gaps are determined by the fifth order of the curvature, $\Delta\omega_\nu^{gap} \propto \kappa_0^5$ with the main gap $\omega_0 \propto 1 - \ell^2\kappa_0^2/2$. In the opposite case, the behavior of the system is changed. The main gap asymptotically closes as $\omega_0 \propto 1/\kappa_0$ and the first one is almost constant. The gaps at higher frequencies $\omega_{\nu\geq2}^{gap} \propto 1/\kappa_0^2$.

4.1.3. Impact of Torsion on Magnon Spectra

In the following, we consider the magnon spectrum of magnetic wires with nonzero curvature and torsion. The key difference to the case of a plane wire with zero torsion is the appearance of the effective magnetic field, described by the vector potential $\mathcal{A}$,

ADVANCED
SCIENCE NEWS

www.advancedsciencenews.com

NANO · MICRO

small

www.small-journal.com

see Equation (35c). The presence of the magnetic field lifts the degeneracy between magnetic excitations along different spatial directions known from planar systems. This aspect was discussed for the case of a helical wire, see Section 3.3.1. Since helices are characterized by the constant curvature and torsion, the corresponding potentials (35) are also constant.[62] Nevertheless, the presence of these potentials drastically changes the magnon spectrum[62]

$$\frac{\omega}{\omega_0} = 2\ell\mathcal{A}k + \sqrt{\left(1 + \ell^2 k^2 + V + \mathcal{A}^2\right)^2 - W^2} \tag{42a}$$

with k being the wave number, see Figure 6h. By analyzing wires with a small curvature and torsion, we can estimate corrections to the case of a straight wire as follows, $\omega \approx \omega_{gap} + \omega_0 \ell^2 (k - \tau)^2$. Similar to a planar curve, the curvature results in the decrease in the gap $\omega_{gap} \approx \omega_0 (1 - \ell^2 \kappa^2/2)$. Unlike a straight wire, the spectrum (42a) is not mirror-symmetric, that is, $\omega(k) \neq \omega(-k)$: the asymmetry of the dispersion curve is caused by the helix torsion. It is described by the vector potential $\mathcal{A}$, which is determined by the curvature-induced DMI. By accounting for the intrinsic DMI, we obtain the following expression for the magnon dispersion law based on the general model of the curved helix wire (26)[93]

$$\omega = \frac{\omega_0}{K}\left[-D_1 k + \sqrt{(Ak^2 + \mathcal{K}_1 + \mathcal{K}_2)(Ak^2 + \mathcal{K}_1)}\right] \tag{42b}$$

We see that the vector potential originates from the mesoscale DMI, $\mathcal{A} \propto D_1$, is responsible for the symmetry break.[62] The latter is similar to the known modification of the spin-wave spectrum in straight systems with the intrinsic DMI[128–130] and nanotubes, where the gap is caused by the curvature.[35,131] The explicit form of the DMI term shows that the corresponding energy gain depends on the product of the geometrical helix chirality $\mathcal{C} = \pm 1$, see Equation (25), and its magnetochirality $\mathfrak{C} = \cos\Phi_0 = \pm 1$.[62]

We note that the magnon spectrum for a helicoid ribbon is also characterized by the non-reciprocity of the spin wave propagation in different directions and the coupling between the geometric and magnetic chiralities.[61] Both properties are examples of geometry-induced chiral symmetry breaking.[30,36]

It is instructive to discuss also the magnon spectrum of helix wires with other directions of the easy-axis anisotropy, which follows the normal and binormal directions. The Frenet equations (2b) are symmetric with respect to the replacement $\kappa \leftrightarrow -\tau$ and $e_T, e_B \leftrightarrow -e_B, e_T$, confer, Equation (5). Thus, the case of the easy axis along e_B can be understood based on the considerations for the easy-tangential one by symmetry considerations. The easy-normal case is qualitatively different. There is the strictly normal state with $\theta = \pi/2$ and $\phi = 0, \pi$ (easy–normal state), preferable for a relatively small curvature and torsion within the range $\kappa < \kappa_c \sqrt{1 - (\tau/\tau_c)^2}$ with $\tau_c \approx 0.67/\ell$.[62] The spin wave spectrum on the background of the easy-normal state

$$\omega = \omega_0 \ell^2 \sqrt{\left(\ell^{-2} + k^2\right)\left(\ell^{-2} + k^2 - \kappa^2 - \tau^2\right)} \tag{43}$$

remains reciprocal[62] since the geometry-induced DMI vector (4) is orthogonal to the ground state magnetization.

4.2. Curvature-Induced Motion of Domain Walls

By considering dynamics of linear excitations (spin waves) in curved wires, we demonstrated that it can be strongly modified by the curvature and torsion of the wire. This includes bounding of states by the wire bends, which is influenced by the curvature or the nonreciprocity of the spin wave radiation, affected by the wire torsion. In this subsection, we discuss the dynamics of nonlinear topological excitations (domain walls) in curved wires. Typically, the motion of domains walls is induced externally by applying magnetic fields or spin-polarized currents. Here, we consider effects of the internal-to-the-system eigenmotion and geometry-induced motion of a domain wall.

First, we discuss the effect of the domain eigenoscillations, which is analogous to the magnon mode bounding problem. Previously in Section 3.2.3 we considered the impact of the spatially inhomogeneous curvature on the equilibrium properties of domain walls: the curvature can pin domain walls at its local extrema. The dynamics of domain walls in curvilinear wires/ribbons is governed by the phenomenological LLG equation (33). By applying the q-Φ model (21) to a curved ribbon, one can integrate out the domain wall profile and set the dynamical problem in terms of the collective variables $\{q, \Phi\}$.[95,106]

$$\frac{\alpha}{\Delta}\dot{q} + p\dot{\Phi} = -2\pi p\omega_0 \ell^2 \frac{\partial \kappa(q)}{\partial q}\cos\Phi$$

$$p\dot{q} - \alpha\Delta\dot{\Phi} = -2\pi p\omega_0 \ell^2 \kappa(q)\sin\Phi + \frac{K_3}{2K_1}\omega_0\Delta\sin 2\Phi \tag{44}$$

where K_1 and K_3 determine coefficients of the easy-axis and easy-plane anisotropy of the ribbon, see Equation (13d). In equilibrium, the domain wall is pinned at a certain position. In the limiting case of uniaxial wires with $K_3 = 0$, the equilibrium position q_0 and phase Φ_0 are determined by the condition (23). By introducing small harmonic decaying oscillations from the equilibrium positions, $q(t) = q_0 + \tilde{q}e^{-\eta t}\sin\omega t$ and $\Phi(t) = \Phi_0 + \tilde{\Phi}e^{-\eta t}\cos\omega t$, it is possible to derive the eigenfrequency of the domain wall and the effective domain wall friction. In the case of the uniaxial wire, the domain eigenfrequency ω and the effective friction η reads, respectively[95]

$$\omega \approx 2\pi\omega_0 \ell^2 \sqrt{\kappa(q_0)|\kappa''(q_0)|}, \qquad \eta \approx \alpha\pi\omega_0\ell\kappa(q_0) \tag{45}$$

Domain wall eigenoscillations can be excited by an external magnetic field pulse as discussed for the case of the parabolic wire bend.[95]

Let us consider now effects of the curvature gradient. Following the set of Equations (44), the curvature gradient through the exchange-induced DMI creates a driving force for domain walls. Thus, in curvilinear wires with $\kappa' \neq 0$ domain walls are moving without any external drive (magnetic field or spin-polarized current) to the region, where curvature reaches its extreme values.

In the particular case of the Cornu spiral (also known as clothoid or Euler's spiral), see **Figure 7a,b**[88]

$$\gamma(s) = \hat{x}\int_0^s d\zeta\cos\left(\frac{\chi}{s}\zeta^2\right) + \hat{y}\int_0^s d\zeta\sin\left(\frac{\chi}{s}\zeta^2\right) \tag{46}$$
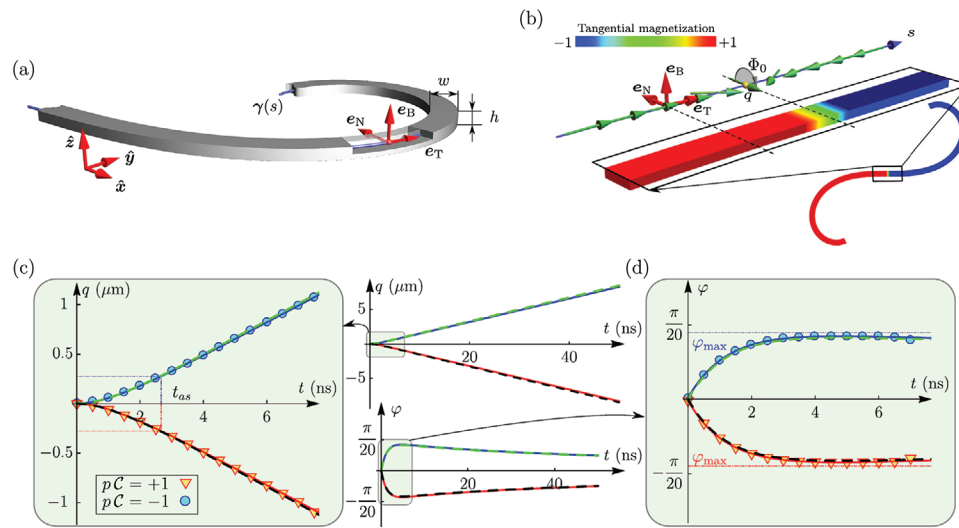
Figure 7. Geometry-induced motion of magnetic domain walls in nanostripes. a) Schematics of a Cornu spiral with relevant geometrical notations. b) Illustration of a 1D head-to-head domain wall ($p = +1$ and $\mathfrak{C} = -1$) in a Cornu spiral described by the two collective variable: the domain wall position q and its relative phase $\varphi = \Phi - \Phi_0$. Red axes determine the curvilinear TNB basis. Green arrows and color scheme determine the magnetization distribution in the stripe obtained in micromagnetic simulations. c,d) A typical behavior of the domain wall position and the phase deviation for a head-to-head domain wall ($p = +1$), respectively. Geometrical parameters of the Cornu spiral are as follows: $\chi \ell^2 = 2 \times 10^{-4}$, $w = 15$ nm, $h = 5$ nm. Solid and dashed lines correspond to the solution of the collective variable Equation (44) and predictions of the linearized model,[106] respectively. Symbols depict the results of micromagnetic simulations. Reproduced with permission.[106] Copyright 2018, American Physical Society.

where the curvature is a linear function of the arc length coordinate, $\kappa(s) = \chi s$, with $\chi = \kappa' = \text{const}$ being the curvature gradient. In this case, using a small-angle approximation for the relative phase of the domain wall $\varphi = \Phi - \Phi_0 \ll 1$ and taking into account that $\alpha \ll 1$, the domain wall speed is found to be constant with its asymptotic expression, see Figure 7c

$$\dot{q} = -2\pi p \mathfrak{C} \omega_0 \ell^2 \frac{\chi}{\alpha} \tag{47}$$

where $\mathfrak{C} = \cos \Phi_0 = \pm 1$ with Φ_0 being the initial domain wall phase. The phase during the dynamics behaves as $\Phi \approx \Phi_0 + p/(\alpha \dot{q} t)$, which results in the long time approximation $\Phi(t \to \infty) = \Phi_0$, see Figure 7d. Hence, the parameter $\mathfrak{C}$ can be interpreted as the domain wall magnetochirality.[132] The corresponding curvature-induced domain wall velocity for the Cornu spiral reaches up to 150 m s^{-1}, while the direction of motion is determined by the sign of the product $p\mathfrak{C}\chi$. During the domain wall motion into the area of larger curvatures, the third term in the energy (22) becomes dominant, which fixes the domain wall phase at $\Phi = 0$ or $\Phi = \pi$ depending on the sign of the product between the polarity p and curvature $\kappa(q)$. Thus, the transition to the precessional regime becomes suppressed, which denotes the curvature-induced suppression of the Walker limit.[106] This contrasts with the case of the field-driven domain wall in a rectilinear wire, where the domain wall phase Φ is not fixed and the Walker limit is present.[109,133]

It should be noted that the velocity (47) is similar to the domain wall velocity $V^u = u\beta/\alpha$ found in magnetic stripes with biaxial anisotropy[134] for the spin-polarized current driving via the Zhang–Li mechanism,[135,136] where β is the nonadiabatic spintransfer parameter. The current-induced translational domain wall motion takes place only if $u < u_w$, where u_w is the

Walker current value.[134,137] However, for the case of a curvature-induced motion, the effect of the Walker-limit transition from the translational to the precessional regimes does not appear in magnetic stripes and the domain wall demonstrates a high-speed translational motion without any external drive.

The curvature-induced motion of transversal domain walls described by the set of equations (44) can be compared with the domain wall automotion observed in curved systems,[138–140] which can be realized due to the following mechanisms: i) the transition from the transverse domain wall to the vortex type after the action of a current pulse;[138] ii) the domain wall motion in curvilinear systems with coordinate-dependent cross-sectional area, due to the magnetostatic interaction and minimization of the total domain wall energy in the narrow areas of asymmetric rings.[139,140]

The influence of the curvature-induced DMI was studied very recently for the domain walls in Permalloy strips patterned as Archimedean spirals with varying widths: according to the experiment, the local variation of the curvature leads to hysteresis loops with stepped behavior.[141]

5. Curvilinear Wires for Spintronic and Spin-Orbitronic Applications

The magnetic responses of curvilinear wires are distinct from their straight counterparts. Namely, intrinsically achiral curved wires behave as a biaxial chiral magnet. The interplay between the intrinsic and curvature-induced extrinsic DMI may make the quasi-tangential state in the wire unstable. These conclusions are based on the analysis of the energy functional (1). Alternatively, curvature effects can emerge in the equation of motion (33) via the symmetry of spintransfer and spin-orbit

ADVANCED
SCIENCE NEWS
www.advancedsciencenews.com

NANO · MICRO
small
www.small-journal.com

torques, which are in the heart of the technological field of spintronics and spin-orbitronics.

Spin-orbit torques, acting on magnetic textures in low-dimensional magnets, see the last term T in Equation (33), can be classified by their symmetry independent of their microscopic origin. The field-like (perpendicular) torques can be produced by the spin Hall effect or Rashba effect.[142] The antidamping-like (Slonczewski) torques also appear as the result of the spin Hall effect or due to the indirect Rashba effect.[142,143] Depending on the type of the wall and the current injection geometry, they can result in a steady motion of the domain wall. It is natural to consider a current direction along a curvilinear wire. It is established that for the case of plane systems, neither the field-like nor antidamping-like torques do lead to the dynamics of the head-to-head (tail-to-tail) walls.[142] The situation is qualitatively different in curvilinear systems.

5.1. Dynamics of Transversal Domain Walls Induced by the Rashba Spin-Orbit Torque

We start with the discussion of the field-like torque in Rashba spin-orbit systems[144] realized by a strong spin-orbit interaction between the nonmagnetic adjacent conductive and ferromagnetic layers. Then, the Rashba field[142]

$$H^R = \frac{\rho P}{\mu_B M_s}\left[j \times e_N\right] \tag{48}$$

with ρ being the Rashba parameter, P being the polarization of carriers in the ferromagnetic layer and $j \parallel e_T$[145] being the charge current. In this geometry, the Rashba field is always directed perpendicular to the wire and cannot push the domain wall in the case of $\kappa = \tau = 0$.[142]

In contrast, for a curvilinear geometry, the equilibrium magnetization direction deviates from the wire direction. This can be realized already in a prototypical example of a helical wire, considered in Section 3.3.1. The simultaneous influence of the curvature and torsion in a helix wire causes the tilt of the ground state magnetization in the rectifying plane by some angle (27a). This leads to the appearance of the magnetization component along the Rashba field, which allows for an efficient displacement of the wall using the spin-orbit Rashba torque. In the case of $\kappa, |\tau| \ll 1/\ell$ and weak enough fields (far below the Walker limit), we can neglect the dynamical change of domains and the internal structure of the wall due to the binormal component of H^R. Within this assumption, it is sufficient to take into account only the component $H_\parallel = H^R \sin\psi$ oriented along the magnetization in the domain. This field component is responsible for the domain wall motion. This allows to use the generalized q-Φ model (30), originally proposed in ref. [114] to describe effects of the intrinsic DMI in biaxial stripes. Finally, being driven by the Rashba torque, the domain wall performs a stationary motion with a finite velocity,[64] see **Figure 8**

$$\dot{q} \approx \frac{2\ell^2}{\gamma_0\alpha}p\kappa\tau H^R \tag{49}$$
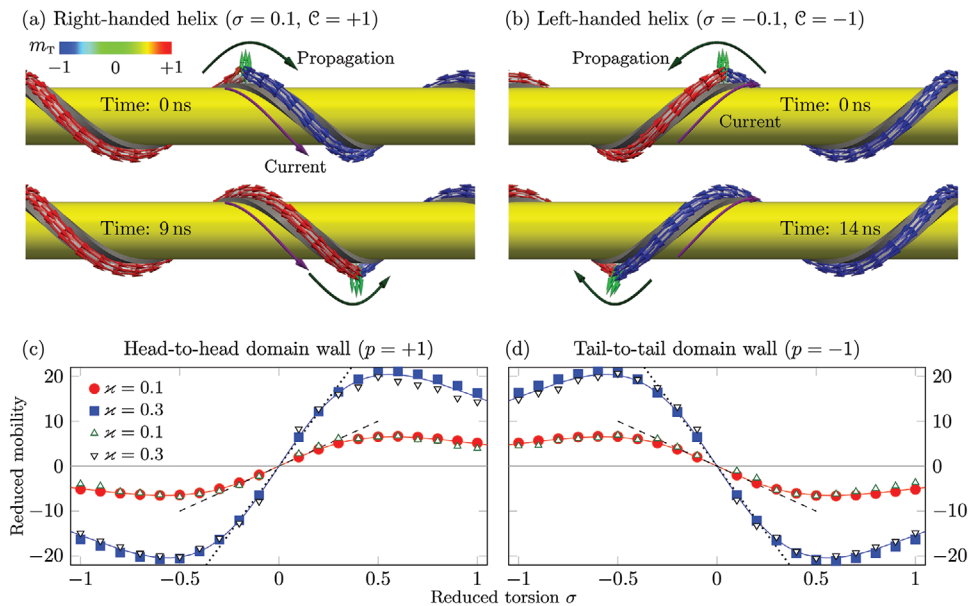

Figure 8. Rashba spin-orbit torque driven transversal domain walls in helix wires. Propagation of the head-to-head domain wall (light-green arrows of magnetization) in a) right-handed and b) left-handed helices with the reduced curvature $\varkappa = \kappa\ell$ and torsion $\varsigma = \tau\ell$, respectively. In both cases, the electric current (burgundy arrow) flows from left to right. The direction of motion of the domain wall (dark green arrow) coincides with current for the right-handed helix. For the left-handed helix, the domain wall moves in the opposite direction. The direction of magnetization inside domains is shown by red and blue arrows. Reduced mobility $\dot{q}/(\gamma_0\ell H^R)$ for the c) head-to-head and d) tail-to-tail domain walls. Dashed lines, open symbols and closed symbols correspond to analytics (49), micromagnetic, and spin-lattice simulations, respectively. Solid lines correspond to the analytical prediction $\dot{q} = 2\pi H^R\Delta\sin\psi/[\alpha\gamma_0(1+\Delta^2\Upsilon^2)]$.[64] Reproduced under the terms of the CC BY Creative Commons Attribution 4.0 International License (http://creativecommons.org/licenses/by/4.0/).[64] Copyright 2016, Springer Nature.
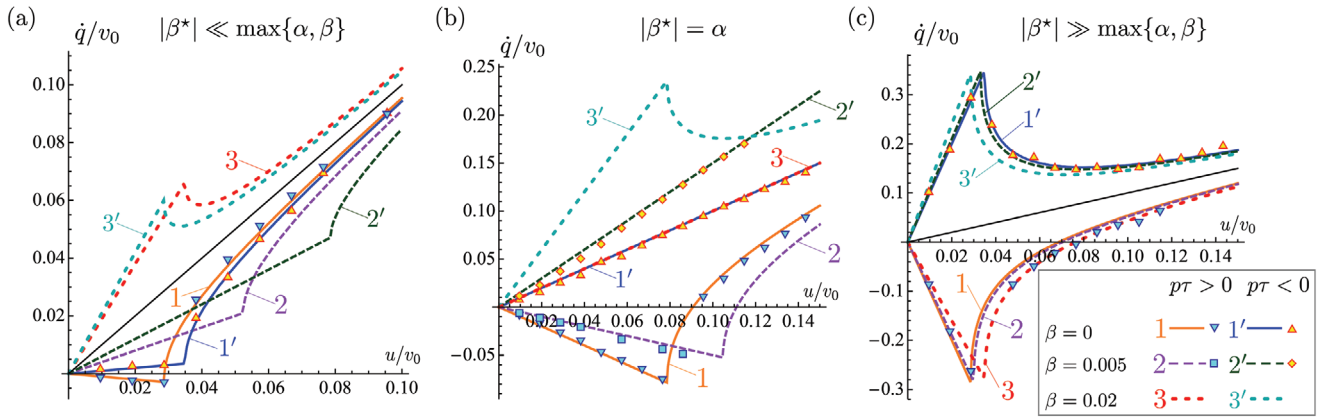
Figure 9. Zhang–Li spintransfer torque driven transversal walls in helix wires. Average velocity of the domain wall $\dot{q}$ as a function of current in units of $v_0 = \gamma_0 \sqrt{4\pi A}$ for helix wires with $\alpha = 0.01$, a) curvature $\kappa = 0.01/\ell$, torsion $\tau = 0.0005/\ell$, and $|\beta^\star| = 0.001$, b) curvature $\kappa = 0.05/\ell$, torsion $\tau = 0.005/\ell$, and $|\beta^\star| = 0.01$, c) curvature $\kappa = 0.1/\ell$, torsion $\tau = 0.05/\ell$, and $|\beta^\star| = 0.1$. Symbols in (a–c) correspond to the data obtained by means of micromagnetic simulations, and lines correspond to the numerical solution of equations of motion, for detail see ref. [63]. Reproduced with permission.[63] Copyright 2016, American Physical Society.

Therefore, the simultaneous impact of the curvature and torsion on the domain wall result in its motion driven by the field-like torque for an intrinsically achiral ferromagnetic wire ($\dot{q} \propto \kappa\tau$). The direction of motion is dependent on the helix chirality $\mathcal{C}$. For example, the head-to-head domain wall follows the direction of the current for the left-handed helix ($\mathcal{C} = 1$, $\tau > 0$) and moves in the opposite direction for the right-handed helix ($\mathcal{C} = -1$, $\tau < 0$).

5.2. Dynamics of Transversal Domain Walls Induced by the Zhang-Li Spintransfer Torque

The mutual influence of the field-like and antidamping-like torques can be illustrated by considering the Zhang–Li mechanism in Equation (33) with the torque[134–136]

$$\boldsymbol{T} = \boldsymbol{m} \times [\boldsymbol{m} \times (\boldsymbol{u} \cdot \nabla)\boldsymbol{m}] + \beta \boldsymbol{m} \times (\boldsymbol{u} \cdot \nabla)\boldsymbol{m} \qquad (50)$$

The quantity $\boldsymbol{u} = j\dfrac{P\mu_B}{|e|M_s}$ with e being the electron charge is close to the average electron drift velocity for the given current density $j \parallel \boldsymbol{e}_T$. The strength of the nonadiabatic antidamping-like spin torque (last term in Equation (50)) is determined by the nonadiabatic spintransfer parameter β. Here, we limit our discussion by considering effects, linear with respect to torsion. In this case, the ψ-frame coincides with the TNB reference frame up to higher terms in torsion and curvature. To describe the domain wall dynamics, we apply the collective variables approach for the ansatz (30) with respect to the extended set of collective variables $\{q(t), \Phi(t), \Delta(t), Y(t)\}$. This system possesses the Walker limit, determined by both the curvature and torsion[63]

$$u_w \approx 2\pi\omega_0\ell^2 \frac{\alpha\kappa}{\alpha - \beta + \beta^*}, \quad \beta^* \approx p\tau\ell \qquad (51)$$

For $u < u_w$, the domain wall velocity reads

$$\dot{q} \approx u \frac{\beta - \beta^*}{\alpha} \qquad (52)$$

The nonzero torsion renormalizes the intrinsic coefficient of nonadiabaticity β by the effective coefficient $\beta - \beta^\star$.

The domain wall reveals a precessional motion above the Walker limit with the frequency $\omega \propto (\beta^\star - \beta - \alpha)\sqrt{u^2 - u_w^2}$. As follows from Equation (51), the domain wall velocity can be tailored in a wide range via the wire geometry. The direction of motion is given by the sign of the term $\alpha - \beta + \beta^\star$. The change of the torsion allows to explore the interplay between the intrinsic Gilbert damping α and the coefficient of nonadiabaticity β. The domain wall always moves in the direction of $\boldsymbol{u}$ for $p\tau < 0$. The behavior of the system is qualitatively different for $p\tau > 0$: i) For $\beta \ll |\beta^\star|$, the domain wall has negative mobility ($\dot{q} < 0$); ii) If $|\beta^\star| \max\{\alpha, \beta\}$, the influence of the nonadiabatic term β vanishes; iii) There is a special value of current above the Walker limit, which leads to the oscillatory motion with zero average velocity. This makes the domain wall dynamics different compared to the case of a planar straight biaxial magnet, see **Figure 9**. We note that the inhomogeneous curvature leads to the pinning of the domain wall at the maximum of κ[42,95] and the Walker-free motion when driven by the effective field (15).[106]

6. Artificial Magnetoelectric Materials with Curvilinear Helimagnets

The link between the geometry and the magnetic order parameter enables new concepts of magnetic memory, logic, and sensor devices.[67,68,95,106,146] Furthermore, the shape of a mechanically flexible wire with coupled magnetic and mechanical subsystems can be controlled through the change of the magnetic ground state, see **Figure 10**a. This effect[67,68] opens appealing perspectives for magnetic soft robot applications, see Section 7. In the case of stiff magnetic nanowires, it is possible to utilize the inverse principle and control the magnetic equilibrium states through tiny geometrical deformations. This is the concept of artificial magnetoelectric materials that offers a new approach to the electric field controlled nanomagnets.[146] The concept relies on the use of geometrically curved
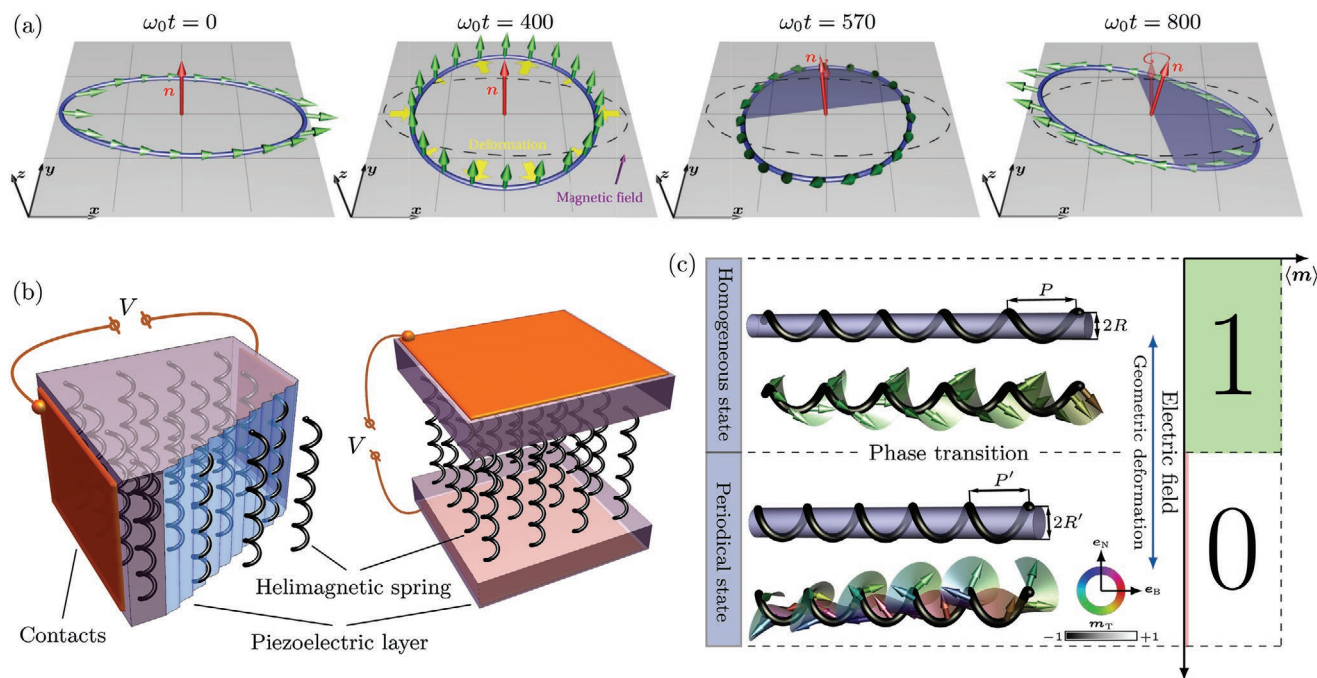
**ADVANCED
SCIENCE NEWS**

www.advancedsciencenews.com

NANO · MICRO

small

www.small-journal.com

Figure 10. The interplay between magnetic and geometric subsystems. a) Temporal profile of mechanical deformations of a flexible magnetic ring exposed to an external magnetic field and mechanical stress, with a subsequent relaxation to the rotated onion state. Green arrows show the magnetization distribution in the stripe obtained in micromagnetic simulations. The red arrow determines the direction of the normal vector **n** to the ring plane. Yellow arrows show directions of mechanical deformations in the plane. The black dashed ellipse ring corresponds to the initial shape of the ring. Reproduced with permission.[67] Copyright 2019, American Physical Society. b) Sketch of magnetoelectric heterostructures based on curvilinear helimagnets embedded in (left) or sandwiched between (right) piezoelectric layers. c) Schematic illustration of the operation principle of the artificial magnetoelectric material based on curvilinear helimagnet represented with helix wires with an intrinsic DMI: by applying voltage to the piezoelectric material, the geometry of the helix (torsion and curvature) are modified. The initial geometry of the helix is adjusted to be close to the helimagnetic phase transition between the quasi-tangential and periodic magnetic state. In this case, even upon small mechanical deformation of the entire system, the average magnetization over the helix wire changes from nonzero value for the quasi-tangential magnetic state to zero for the periodic state. This system offers a large converse magnetoelectric effect. (b) and (c) adapted with permission.[146] Copyright 2019, IOP Publishing Ltd.

helimagnets embedded in a piezoelectric matrix or sandwiched between piezoelectric layers, see Figure 10b. Applying the electric field to the piezoelectric material introduces geometrical deformations of the curvilinear helimagnet, which in turn leads to the reversible magnetic phase transition between two types of magnetic textures: quasi-tangential and periodic magnetic states,[93] see Figure 10c. This transition is caused by the change of the mesoscale DMI constant through the critical value by modifying the geometrical parameters of the helimagnet.

A spring-shaped helimagnetic nanowire, see Section 3.3.1, is a prototypical example of the proposed concept as it has well-defined transition region between the periodic (28) and quasi-tangential (27) magnetic states.[93] This transition is characterized by the change of the average remnant magnetization along the helix symmetry axis $\langle M \rangle$. In the case of the periodic state, due to the magnetization modulations along the nanospring and geometrical modulations of the spring itself, the average normalized remanent magnetization $\langle M \rangle = 0$. Oppositely, in the case of the quasi-tangential magnetic distribution, the average net magnetization over the spring reads

$$\langle M \rangle = \hat{z} M_s \sin\left(\psi + \arctan\frac{\tau}{\kappa}\right) \tag{53}$$

where ψ determines the tilt angle of the magnetization distribution, see Equation (27a), and the second part corresponds to the geometrical inclination of the helimagnetic spring. As a result, upon the phase transition, the average remanent magnetic moment of the system changes from nonzero in the quasi-tangential state, see Figure 10c, to zero value in the periodically modulated state of the helimagnet, see Figure 10c. This describes the basic functionality of the proposed magnetoelectric memory device, with an electric field controlled binary switching from "1" to "0" and vice versa, see Figure 10c.

The proposed concept of artificial magnetoelectric material relies on the converse magnetoelectric effect, which is defined as the change in the magnetic moment responding to the applied electric field, which could be quantified as follows

$$\lambda_{CME} = \langle \Delta M \rangle d_{33}/\delta \tag{54}$$

where $\langle \Delta M \rangle$ is the change of the average magnetic moment over the nanospring, d_{33} is the piezoelectric coefficient and δ denotes a linear relative change of the geometrical parameters ($R \rightarrow R'$ and $P \rightarrow P'$) during the deformation: $P' = (1 - \delta)P$ and $R' = R/\sqrt{1-\delta}$. For a Co/Pt-based multilayer system with $M_s = 1.1 \times 10^6$ A m^{-1} embedded in a PZT matrix with $d_{33} = 0.5$ nm V^{-1}

and linear deformation $\delta = 2\%$ the resulting magnetoelectric coefficient is $\lambda_{CME} = 15 \times 10^{-3}$ (A m^{-1})/(V m^{-1}). This is a significant enhancement of the converse magnetoelectric coefficient compared to the common magnetoelectric systems: multiferroic ceramics ($\lambda_{CME} = 3.2 \times 10^{-8}$ (A m^{-1})/(V m^{-1}) for BaTiO$_3$-BiFeO$_3$ single phase system[147]) and laminated composites ($\lambda_{CME} = 2.9 \times 10^{-3}$ (A m^{-1})/(V m^{-1}) for PMN-PT single crystal and Terfenol-D alloy composites[148]).

7. Mechanically Flexible and Elastic Curvilinear Magnetic Wires

Magnetic soft matter opens new possibilities in design and fabrication of shapeable magnetoelectronics,[149–151] and programmable magnetic materials.[152–156] The possibility of the remote control of the shape and 3D navigation of soft magnets relying on external magnetic fields stimulates intensive investigations in the area of milli-[152,153,157] and microrobotics.[27,158–161] For nanomagnets with the dominant short-range exchange interaction, the deformations are assumed to be at the nanoscale range. This allows significantly reduce the size of the object and opens new perspectives in the development of nanorobots.[162]

In the following, we discuss the generalization of the model of a rigid curved wire presented in Section 2 to describe mechanically flexible magnetic systems. The minimal extension can be done by adding bending energy of the wire,[89] which results in[67]

$$E = \int \left[A\boldsymbol{m}'^2 - K(\boldsymbol{m} \cdot \boldsymbol{v})^2 + B\boldsymbol{v}'^2 \right] \mathrm{d}\boldsymbol{r} \tag{55}$$

The bending is described by the last term with B being the bending constant and $\boldsymbol{v}$ being the tangential vector, which can be referred to as the elastic vector with a constraint $|\boldsymbol{v}| = 1$. The bending parameter B for the wire of thickness h can be expressed through its Young's modulus Y as $B = Yh^2/8$.[163] In the case of the angular parametrization for the magnetization and elastic vectors in the form $\boldsymbol{m} = (\sin\theta\cos\phi, \sin\theta\sin\phi, \cos\theta)$ and $\boldsymbol{v} = (\sin\psi\cos\chi, \sin\psi\sin\chi, \cos\psi)$, the energy density in the expression (55) reads

$$\mathcal{E} = A\left\{ \theta'^2 + \sin^2\theta\phi'^2 - \left[\sin\theta\sin\psi\cos(\phi-\chi) + \cos\theta\cos\psi \right]^2 \right\} + B\left(\psi'^2 + \sin^2\psi\chi'^2 \right) \tag{56}$$

7.1. Equilibrium States of Flexible Rings

To illustrate new effects, which appear in a flexible wire, we discuss a closed wire.[67] The equilibrium states of a flexible 1D wire are determined by the minimum of the energy functional (56). These states correspond to the planar magnetization distribution in a planar wire with the magnetization vector $\boldsymbol{m}$ lying within the wire plane

$$\boldsymbol{m}_0 = (\cos\phi_0, \sin\phi_0, 0), \quad \boldsymbol{v}_0 = (\cos\chi_0, \sin\chi_0, 0) \tag{57}$$

The azimuthal magnetic angle ϕ_0 and the corresponding elastic angle χ_0 are determined by the set of two coupled pendulum equations

$$2\ell^2\phi_0'' - \sin 2(\phi_0 - \chi_0) = 0, \quad 2\beta\ell^2\chi_0'' + \sin 2(\phi_0 - \chi_0) = 0 \tag{58}$$

with $\beta = B/A$ being the dimensionless bending parameter. The set of Equations (58) describes a flux-free magnetization distribution (vortex state) in a circular wire[67]

$$\phi_0^{\mathrm{vor}} = \chi_0^{\mathrm{vor}} = 2\pi s/L \tag{59a}$$

see **Figure 11**a. This solution is similar to the vortex state in a rigid ring.[60] Besides, there exists the onion solution[67]

$$\phi_0^{\mathrm{on}} = \frac{\beta}{1+\beta}\left[2\pi\frac{s}{L} - \frac{\pi}{2} - \mathrm{am}\left(\frac{4K(k)}{L}s, k \right) \right],$$
$$\chi_0^{\mathrm{on}} = \frac{1}{1+\beta}\left[2\pi\beta\frac{s}{L} + \frac{\pi}{2} + \mathrm{am}\left(\frac{4K(k)}{L}s, k \right) \right] \tag{59b}$$

where the modulus k is determined by the equation $4\ell\sqrt{k}K(k) = L\sqrt{(1+\beta)/\beta}$. The magnetic structure of the onion solution is similar to the onion state in a rigid ring. As a result of the coupling between magnetic and mechanical subsystems, in the magnetic onion state the wire becomes elliptically deformed, see Figure 11b. By comparing energies of the vortex and onion states, we conclude that the vortex state in a circular-shaped ring is realized for a relatively large L: such a state minimizes the anisotropy energy. Instead, the onion state is realized for small rings and small bending parameter, supported by the exchange interaction,[67] see Figure 11c. The boundary between the vortex and onion states in a flexible ring can be approximated as

$$\frac{2\pi}{L} = \kappa_0 \frac{\sqrt{c^2 + 1/\beta}}{c + \pi\kappa_0\ell/(4\beta)}, \quad c \approx 1.106 \tag{60}$$

Here, $\kappa_0 \approx 0.657/\ell$ is a dimensionless curvature for a rigid ring, which separates the onion and vortex states, see Section 3.2.1 for details. It should be noted that phase diagram presented in Figure 11c shows the equilibrium states in elastic ring. However, one can obtain the metastable states: i) onion state in elliptically-like deformed ring in the vortex area; ii) vortex state in circular ring in the onion area.

7.2. Zero Modes of Flexible Rings

The energy (55) is invariant with respect to the joint rotation of the elastic $\boldsymbol{v}$-vector and the magnetization $\boldsymbol{m}$-vector by the angle Ω about the axis given by $\boldsymbol{g} = (\sin\psi_g\cos\chi_g, \sin\psi_g\sin\chi_g, \cos\psi_g)$

$$\boldsymbol{v} \to U^g(\Omega)\boldsymbol{v}, \quad \boldsymbol{m} \to U^g(\Omega)\boldsymbol{m},$$
$$U^g(\Omega) = (1 - \cos\Omega)\boldsymbol{g}\,\boldsymbol{g}^\top + \cos\Omega\mathbb{1} + \sin\Omega g^\times \tag{61}$$

Here, $U^g(\Omega)$ is the rotation matrix,[164] $\mathbb{1}$ is the identity matrix, and elements of the matrix $g^\times$ are defined as $g_{ij}^\times = -\varepsilon_{ijk}g_k$. A consequence of this rotational symmetry is the appearance of normal modes with zero frequency (zero modes) on the background of the equilibrium states (57). The corresponding elastic zero mode, as a linear excitation $\Delta\boldsymbol{u}$ on the background of the
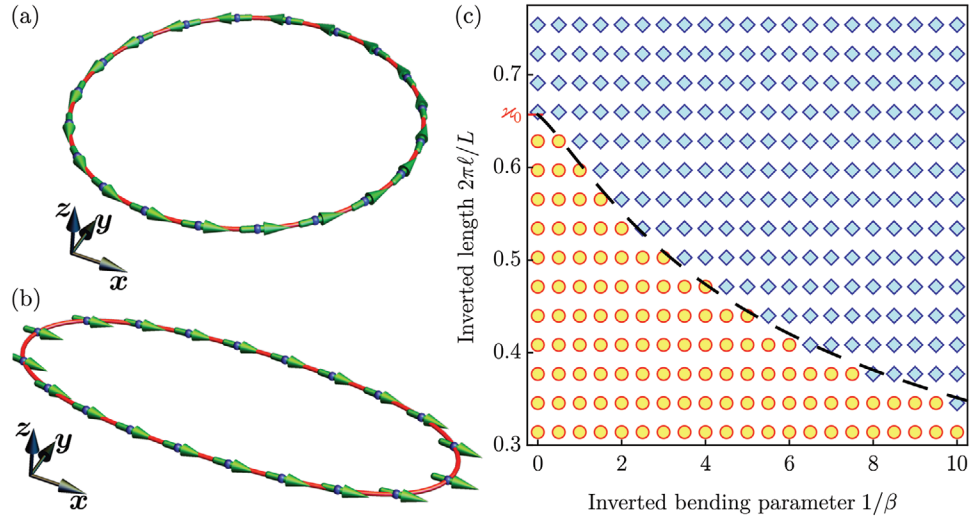
Figure 11. Equilibrium states of flexible ferromagnetic rings. a) Magnetic vortex state in a wire of circular shape. b) Magnetic onion state in a wire of elliptical shape. In (a) and (b), green arrows show the magnetization distribution in the wire obtained in numerical simulations. Equilibrium state is determined by the geometrical and material parameters of the wire, that is, for relatively large ring and bending parameter the vortex state in circular wire (a) is preferable, and for relatively small rings and bending parameters—onion state (b). c) Phase diagram of the equilibrium magnetization and shape states for a flexible ferromagnetic ring. Symbols correspond to simulation: blue diamonds correspond to the onion state shown in (b); yellow circles correspond to the vortex state shown in (a). Dashed line in (c) is plotted according prediction (60). Reproduced with permission.[67] Copyright 2019, American Physical Society.

static solution $\boldsymbol{v}_0$, that is, $\Delta\boldsymbol{v} = \boldsymbol{v} - \boldsymbol{v}_0$, is determined by the infinitesimal rotation

$$\Delta\boldsymbol{v} \propto \partial_\Omega U^g(\Omega)\boldsymbol{v}_0(s)\big|_{\Omega=0} = \left\| \begin{matrix} -\cos\psi_g\sin\chi_0 \\ \cos\psi_g\cos\chi_0 \\ \sin\psi_g\sin(\chi_0-\chi_g) \end{matrix} \right\| \tag{62}$$

In the same way, we can derive the magnetic zero mode, $\Delta\boldsymbol{m} \propto \partial_\gamma U^g(\Omega)\boldsymbol{m}_0(s)\big|_{\Omega=0}$. In terms of angular variables, the zero mode solutions read

$$\Delta\psi = c_1\sin(\chi_0-\chi_g), \quad \Delta\chi = c_2,$$
$$\Delta\theta = c_1\sin(\chi_0-\chi_g), \quad \Delta\phi = c_2 \tag{63}$$

where χ_g is a constant angle; c_1 and c_2 describe amplitudes of the corresponding modes. By exciting zero modes, we can turn the loop plane by some angle, see Figure 10a.

8. Conclusions

This review summarizes current research activities of 1D curvilinear magnetic wires (plane and space curves). A curvilinear geometry brings about biaxial anisotropy and DMI, which can interplay with the intrinsic anisotropy and DMI. In this respect, magnetic responses of curvilinear helimagnetic wires are determined by the mesoscale anisotropy and DMI and can be tuned by changing the geometrical parameters of the object, namely curvature and torsion of the wire as well as closeness of the curve. 1D systems allow for intuitive understanding of the curvilinear effects and can be used for numerous practical

estimations, for example, geometry-induced helimagnetic transition, Rashba field driven motion of transversal domain walls, quantification of band gaps for curvilinear magnonic crystals and dispersion of spin waves in curved wires.

We consider curved magnetic wires as a promising system for fundamental research in the field of curvilinear and 3D magnetism, primarily due to the availability of fabrication and characterization techniques, which can finally enable intensive experimental activities with wires of different shape and composition. Prospective fundamental studies of curvilinear magnetic wires include investigations of the dynamics of topological magnetic solitons (e.g., domain walls, kinks) and switching phenomena, which are essential for possible applications in spin-orbitronics and magnonics.[30] Furthermore, it would be important to extend the current theory to tackle the effect of strain in curved wires, which is relevant for any practical assessment of the performance of devices based on these low-dimensional systems. For instance, strain can be used to induce or modify the intrinsic DMI,[165] which can contribute to the mesoscale DMI and anisotropy. We note that the studies of geometrically curved objects with strain could be already done relying on micromagnetic solvers. For instance, magnetoelastic modules are available in a COMSOL code[166–169] and recently included in MuMax3.[170] Still, the current theory of the curvilinear magnetism does not address the effects of strain (or in general magnetomechanics) on the responses of curved thin films and wires. This makes the current theory incomplete and does not allow to have a complete understanding of the processes, which happen for instance in flexible magnetic sensor devices upon mechanical deformation. To this end, it is known that striction effects can have a strong impact on magnetic textures and their behavior of low-dimensional magnetic systems. These effects contribute to and sometimes even govern

the properties of magnetic textures, and hence can influence the sensitivity of magnetic field sensors based on geometrically curved architectures.

At the moment, curvature effects are considered primarily in ferromagnetic systems. It is insightful to address other types of magnetic ordering. In this respect, the concept of curvilinear antiferromagnet has been introduced very recently for curved 1D spin chains.[86] It is demonstrated that an intrinsically achiral 1D curvilinear antiferromagnet behaves as a chiral helimagnet with geometrically tunable DMI, orientation of the Néel vector and the helimagnetic phase transition. Furthermore, the curvature-induced DMI results in the hybridization of spin wave modes and enables a geometrically-driven local minimum of the low frequency branch, which opens exciting perspectives to study long-living collective magnon states in antiferromagnets. This positions curvilinear 1D antiferromagnets as a perspective platform for the realization of geometrically tunable chiral antiferromagnets for antiferromagnetic spinorbitronics and fundamental discoveries in the formation of coherent magnon condensates in the momentum space. An extension of the theory beyond the σ-model allows to describe curvilinear 1D antiferromagnets and determine conditions when they possess the geometry-driven weak ferromagnetism.[171] Furthermore, in contrast to ferromagnets, curvilinear antiferromagnetic spin chains exhibit the geometry-driven modification of the magnetic responses stemming also from the anisotropy interaction.[171] These initial studies open perspectives for utilizing specific features of antiferromagnets in engineering of chiral[172] and anisotropic[173] responses and soliton dynamics[174,175] for applications.

There is still a big gap between the theoretical activities and corresponding experimental realizations. To develop the field of curvilinear and 3D magnetism further, it is important to stimulate and intensify experimental work on the realization of curvilinear wires, characterization of their static and dynamic magnetic responses as well as generating new application scenarios. We are convinced that the full application potential of curvilinear wires is yet to be explored for different device ideas.[30,39–41] The current active application–oriented activities on shapeable magnetoelectronics,[176,177] elastic magnetic field sensorics,[178] spintronics,[14,56,179–184] 3D magnonics,[117–119,122] and related concepts of reservoir computing,[185] magnetosensitive e-skins,[151] magnetic soft robotics,[186,187] trapping magnetic particles and living cells for magnetic sorting and sensing in fluidics, smart micromachines, and active soft matter[27,188] could be used as an inspiration for the implementation of curvilinear magnetic wires in technology.

Conflict of Interest

The authors declare no conflict of interest.

[1] C. Ortix, S. Kiravittaya, O. G. Schmidt, J. van den Brink, *Phys. Rev. B* **2011**, *84*, 045438.

[2] L. C. da Silva, C. C. Bastos, F. G. Ribeiro, *Ann. Phys.* **2017**, *379*, 13.

[3] C. Ortix, *Phys. Rev. B* **2015**, *91*, 245412.

[4] J. P. Baltanás, H. Saarikoski, A. A. Reynoso, D. Frustaglia, *Phys. Rev. B* **2017**, *96*, 035312.

[5] H. Aoki, M. Koshino, D. Takeda, H. Morise, K. Kuroki, *Phys. Rev. B* **2001**, *65*, 3.

[6] C. Ortix, J. van den Brink, *Phys. Rev. B* **2010**, *81*, 165419.

[7] V. M. Fomin, R. O. Rezaev, O. G. Schmidt, *Nano Lett.* **2012**, *12*, 1282.

[8] Z.-J. Ying, M. Cuoco, C. Ortix, P. Gentile, *Phys. Rev. B* **2017**, *96*, 100506(R).

[9] S. Lösch, A. Alfonsov, O. V. Dobrovolskiy, R. Keil, V. Engemaier, S. Baunack, G. Li, O. G. Schmidt, D. Bürger, *ACS Nano* **2019**, *13*, 2948.

[10] Q.-D. Jiang, T. Hansson, F. Wilczek, *Phys. Rev. Lett.* **2020**, *124*, 197001.

[11] Z.-J. Ying, P. Gentile, J. P. Baltanás, D. Frustaglia, C. Ortix, M. Cuoco, *Phys. Rev. Res.* **2020**, *2*, 023167.

[12] C.-H. Chang, J. van den Brink, C. Ortix, *Phys. Rev. Lett.* **2014**, *113*, 22.

[13] P. Gentile, M. Cuoco, C. Ortix, *Phys. Rev. Lett.* **2015**, *115*, 256801.

[14] K. S. Das, D. Makarov, P. Gentile, M. Cuoco, B. J. van Wees, C. Ortix, I. J. Vera-Marun, *Nano Lett.* **2019**, *19*, 6839.

[15] R. Battilomo, N. Scopigno, C. Ortix, *Phys. Rev. Lett.* **2019**, *123*, 196403.

[16] S.-C. Ho, C.-H. Chang, Y.-C. Hsieh, S.-T. Lo, B. Huang, T.-H.-Y. Vu, C. Ortix, T.-M. Chen, *Nat. Electron.* **2021**, *4*, 116.

[17] R. D. Kamien, D. R. Nelson, C. D. Santangelo, V. Vitelli, *Phys. Rev. E* **2009**, *80*, 051703.

[18] X. Zhou, Z. Tian, H. J. Kim, Y. Wang, B. Xu, R. Pan, Y. J. Chang, Z. Di, P. Zhou, Y. Mei, *Small* **2019**, *15*, 1902528.

[19] Y. Wang, Y. Wang, G. Huang, Y. Kong, C. Liu, Z. Zhao, K. Wu, Y. Mei, *Adv. Photonics Res.* **2021**, *2*, 2000163.

[20] S. A. Maier, *Plasmonics: Fundamentals and Spplications*, 1st ed., Springer, Berlin, Heidelberg **2007**.

[21] Y. Yin, S. Li, S. Böttner, F. Yuan, S. Giudicatti, E. S. G. Naz, L. Ma, O. G. Schmidt, *Phys. Rev. Lett.* **2016**, *116*, 25.

[22] H. Vu, J. Siebels, D. Sonnenberg, S. Mendach, T. Kipp, *ACS Photonics* **2017**, *4*, 2659.

[23] *On-Chip Communication Architectures* (Eds: S. Pasricha, N. Dutt), Elsevier, New York **2008**.

[24] D. Nelson, S. Weinberg, T. Piran, *Statistical Mechanics of Membranes and Surfaces (Second Edition)*, World Scientific, Singapore **2004**.

[25] T. Lopez-Leon, V. Koning, K. B. S. Devaiah, V. Vitelli, A. Fernandez-Nieves, *Nat. Phys.* **2011**, *7*, 391.

[26] G. Napoli, L. Vergori, *Phys. Rev. Lett.* **2012**, *108*, 207803.

[27] B. Wang, K. Kostarelos, B. J. Nelson, L. Zhang, *Adv. Mater.* **2020**, *33*, 2002047.

[28] C. K. Schmidt, M. Medina-Sánchez, R. J. Edmondson, O. G. Schmidt, *Nat. Commun.* **2020**, *11*, 5618.

[29] C. C. J. Alcântara, F. C. Landers, S. Kim, C. D. Marco, D. Ahmed, B. J. Nelson, S. Pané, *Nat. Commun.* **2020**, *11*, 5957.

[30] D. D. Sheka, *Appl. Phys. Lett.* **2021**, *118*, 230502.

[31] Y. Gaididei, V. P. Kravchuk, D. D. Sheka, *Phys. Rev. Lett.* **2014**, *112*, 257203.

[32] D. D. Sheka, O. V. Pylypovskyi, P. Landeros, Y. Gaididei, A. Kákay, D. Makarov, *Commun. Phys.* **2020**, *3*, 128.

[33] D. Sander, S. O. Valenzuela, D. Makarov, C. H. Marrows, E. E. Fullerton, P. Fischer, J. McCord, P. Vavassori, S. Mangin, P. Pirro, B. Hillebrands, A. D. Kent, T. Jungwirth, O. Gutfleisch, C. G. Kim, A. Berger, *J. Phys. D: Appl. Phys.* **2017**, *50*, 363001.

[34] E. Y. Vedmedenko, R. K. Kawakami, D. Sheka, P. Gambardella, A. Kirilyuk, A. Hirohata, C. Binek, O. A. Chubykalo-Fesenko, S. Sanvito, B. Kirby, J. Grollier, K. Everschor-Sitte, T. Kampfrath, C.-Y. You, A. Berger, *J. Phys. D: Appl. Phys.* **2020**, *53*, 453001.

[35] R. Hertel, *SPIN* **2013**, *03*, 1340009.

[36] R. Streubel, P. Fischer, F. Kronast, V. P. Kravchuk, D. D. Sheka, Y. Gaididei, O. G. Schmidt, D. Makarov, *J. Phys. D: Appl. Phys.* **2016**, *49*, 363001.

[37] A. Fernández-Pacheco, R. Streubel, O. Fruchart, R. Hertel, P. Fischer, R. P. Cowburn, *Nat. Commun.* **2017**, *8*, 15756.

[38] P. Fischer, D. Sanz-Hernández, R. Streubel, A. Fernández-Pacheco, *APL Mater.* **2020**, *8*, 010701.

[39] R. Streubel, E. Y. Tsymbal, P. Fischer, *J. Appl. Phys.* **2021**, *129*, 210902.

[40] D. Makarov, O. M. Volkov, A. Kákay, O. V. Pylypovskyi, B. Budinská, O. V. Dobrovolskiy, *Adv. Mater.* **2021**, 2101758.

[41] L. J. Heyderman, J. Grollier, C. H. Marrows, P. Vavassori, D. Grundler, D. Makarov, S. Pané, *Appl. Phys. Lett.* **2021**, *119*, 080401.

[42] O. M. Volkov, A. Kákay, F. Kronast, I. Mönch, M.-A. Mawass, J. Fassbender, D. Makarov, *Phys. Rev. Lett.* **2019**, *123*, 077201.

[43] W. Jung, Y.-H. Jung, P. V. Pikhitsa, J. Feng, Y. Yang, M. Kim, H.-Y. Tsai, T. Tanaka, J. Shin, K.-Y. Kim, H. Choi, J. Rho, M. Choi, *Nature* **2021**, *592*, 54.

[44] A. G. Mark, J. G. Gibbs, T.-C. Lee, P. Fischer, *Nat. Mater.* **2013**, *12*, 802.

[45] C. Phatak, Y. Liu, E. B. Gulsoy, D. Schmidt, E. Franke-Schubert, A. Petford-Long, *Nano Lett.* **2014**, *14*, 759.

[46] S. Eslami, J. G. Gibbs, Y. Rechkemmer, J. van Slageren, M. Alarcón-Correa, T.-C. Lee, A. G. Mark, G. L. J. A. Rikken, P. Fischer, *ACS Photonics* **2014**, *1*, 1231.

[47] J. M. D. Teresa, A. Fernández-Pacheco, R. Córdoba, L. Serrano-Ramón, S. Sangiao, M. R. Ibarra, *J. Phys. D: Appl. Phys.* **2016**, *49*, 243003.

[48] D. Sanz-Hernández, R. F. Hamans, J.-W. Liao, A. Welbourne, R. Lavrijsen, A. Fernández-Pacheco, *ACS Nano* **2017**, *11*, 11066.

[49] M. Huth, F. Porrati, O. Dobrovolskiy, *Microelectron. Eng.* **2018**, *185–186*, 9.

[50] R. Winkler, J. D. Fowlkes, P. D. Rack, H. Plank, *J. Appl. Phys.* **2019**, *125*, 210901.

[51] H. Plank, R. Winkler, C. H. Schwalb, J. Hütner, J. D. Fowlkes, P. D. Rack, I. Utke, M. Huth, *Micromachines* **2019**, *11*, 48.

[52] C. Phatak, C. S. Miller, Z. Thompson, E. B. Gulsoy, A. K. Petford-Long, *ACS Appl. Nano Mater.* **2020**, *3*, 6009.

[53] G. Williams, M. Hunt, B. Boehm, A. May, M. Taverne, D. Ho, S. Giblin, D. Read, J. Rarity, R. Allenspach, S. Ladak, *Nano Res.* **2018**, *11*, 845.

[54] S. Sahoo, S. Mondal, G. Williams, A. May, S. Ladak, A. Barman, *Nanoscale* **2018**, *10*, 9981.

[55] J. Askey, M. O. Hunt, W. Langbein, S. Ladak, *Nanomaterials* **2020**, *10*, 429.

[56] F. Meng, C. Donnelly, C. Abert, L. Skoric, S. Holmes, Z. Xiao, J.-W. Liao, P. J. Newton, C. H. W. Barnes, D. Sanz-Hernández, A. Hierro-Rodriguez, D. Suess, R. P. Cowburn, A. Fernández-Pacheco, *ACS Nano* **2021**, *15*, 6765.

[57] D. Sanz-Hernández, A. Hierro-Rodriguez, C. Donnelly, J. Pablo-Navarro, A. Sorrentino, E. Pereiro, C. Magén, S. McVitie, J. M. de Teresa, S. Ferrer, P. Fischer, A. Fernández-Pacheco, *ACS Nano* **2020**, *14*, 8084.

[58] L. Skoric, D. Sanz-Hernández, F. Meng, C. Donnelly, S. Merino-Aceituno, A. Fernández-Pacheco, *Nano Lett.* **2020**, *20*, 184.

[59] P. Pip, C. Donnelly, M. Döbeli, C. Gunderson, L. J. Heyderman, L. Philippe, *Small* **2020**, *16*, 2004099.

[60] D. D. Sheka, V. P. Kravchuk, Y. Gaididei, *J. Phys. A: Math. Theor.* **2015**, *48*, 125202.

[61] Y. Gaididei, A. Goussev, V. P. Kravchuk, O. V. Pylypovskyi, J. M. Robbins, D. Sheka, V. Slastikov, S. Vasylkevych, *J. Phys. A: Mathe. Theor.* **2017**, *50*, 385401.

[62] D. D. Sheka, V. P. Kravchuk, K. V. Yershov, Y. Gaididei, *Phys. Rev. B* **2015**, *92*, 054417.

[63] K. V. Yershov, V. P. Kravchuk, D. D. Sheka, Y. Gaididei, *Phys. Rev. B* **2016**, *93*, 094418.

[64] O. V. Pylypovskyi, D. D. Sheka, V. P. Kravchuk, K. V. Yershov, D. Makarov, Y. Gaididei, *Sci. Rep.* **2016**, *6*, 23316.

[65] Y. Gaididei, V. P. Kravchuk, F. G. Mertens, O. V. Pylypovskyi, A. Saxena, D. D. Sheka, O. M. Volkov, *Low Temp. Phys.* **2018**, *44*, 634.

[66] A. Korniienko, V. Kravchuk, O. Pylypovskyi, D. Sheka, J. van den Brink, Y. Gaididei, *SciPost Phys.* **2019**, *7*, 35.

[67] Y. Gaididei, K. V. Yershov, D. D. Sheka, V. P. Kravchuk, A. Saxena, *Phys. Rev. B* **2019**, *99*, 014404.

[68] K. V. Yershov, V. P. Kravchuk, D. D. Sheka, J. van den Brink, Y. Gaididei, *Phys. Rev. B* **2019**, *100*, 140407(R).

[69] B. Dick, M. J. Brett, T. J. Smy, M. R. Freeman, M. Malac, R. F. Egerton, *J. Vac. Sci. Technol., A* **2000**, *18*, 1838.

[70] B. Dick, M. J. Brett, T. Smy, *J. Vacuum Sci. Technol. B* **2003**, *21*, 23.

ADVANCED
SCIENCE NEWS
www.advancedsciencenews.com

NANO · MICRO
small
www.small-journal.com

[71] J. G. Gibbs, A. G. Mark, T.-C. Lee, S. Eslami, D. Schamel, P. Fischer, *Nanoscale* **2014**, *6*, 9457.

[72] Z. Wu, J. Troll, H.-H. Jeong, Q. Wei, M. Stang, F. Ziemssen, Z. Wang, M. Dong, S. Schnichels, T. Qiu, P. Fischer, *Sci. Adv.* **2018**, *4*, eaat4388.

[73] L. Keller, M. K. I. A. Mamoori, J. Pieper, C. Gspan, I. Stockem, C. Schröder, S. Barth, R. Winkler, H. Plank, M. Pohlit, J. Müller, M. Huth, *Sci. Rep.* **2018**, *8*, 6160.

[74] M. A. Mamoori, L. Keller, J. Pieper, S. Barth, R. Winkler, H. Plank, J. Müller, M. Huth, *Materials* **2018**, *11*, 289.

[75] H. Maurenbrecher, J. Mendil, G. Chatzipirpiridis, M. Mattmann, S. Pané, B. J. Nelson, P. Gambardella, *Appl. Phys. Lett.* **2018**, *112*, 242401.

[76] V. Magdanz, M. Medina-Sánchez, L. Schwarz, H. Xu, J. Elgeti, O. G. Schmidt, *Adv. Mater.* **2017**, *29*, 1606301.

[77] M. Medina-Sánchez, L. Schwarz, A. K. Meyer, F. Hebenstreit, O. G. Schmidt, *Nano Lett.* **2016**, *16*, 555.

[78] K. Kobayashi, K. Ikuta, in *2009 IEEE 22nd International Conference on Micro ElectroMechanical Systems*, IEEE, Piscataway, NJ **2009**, pp. 11–14.

[79] V. V. Slastikov, C. Sonnenberg, *IMA J. Appl. Math.* **2012**, *77*, 220.

[80] T. Moriya, *Phys. Rev.* **1960**, *120*, 91.

[81] I. E. Dzyaloshinskii, *Sov. Phys. JETP* **1964**, *19*, 960.

[82] I. E. Dzyaloshinskii, *Sov. Phys. JETP* **1965**, *20*, 223.

[83] S. Rohart, A. Thiaville, *Phys. Rev. B* **2013**, *88*, 184422.

[84] E. J. Smith, D. Makarov, S. Sanchez, V. M. Fomin, O. G. Schmidt, *Phys. Rev. Lett.* **2011**, *107*, 097204.

[85] *Handbook of Magnetism and Advanced Magnetic Materials*, Vol. *2* (Eds: H. Kronmüller, S. Parkin), Wiley-Interscience, Hoboken, NJ **2007**.

[86] O. V. Pylypovskyi, D. Y. Kononenko, K. V. Yershov, U. K. Rößler, A. V. Tomilo, J. Fassbender, J. van den Brink, D. Makarov, D. D. Sheka, *Nano Lett.* **2020**, *20*, 8157.

[87] W. Kühnel, *Differential Geometry: Curves–Surfaces–Manifolds*, American Mathematical Society, Providence, RI **2015**.

[88] E. W. Weisstein, *The CRC Concise Encyclopedia of Mathematics*, Chapman & Hall/CRC, Boca Raton, FL **2003**.

[89] R. Kamien, *Rev. Mod. Phys.* **2002**, *74*, 953.

[90] J. Fernandez-Roldan, Y. Ivanov, O. Chubykalo-Fesenko, in *Magnetic Nano- and Microwires*, Elsevier, New York **2020**, pp. 403–426.

[91] B. Göbel, I. Mertig, O. A. Tretiakov, *Phys. Rep.* **2021**, *895*, 1.

[92] *Magnetic Nano- and Microwires*, 2nd ed. (Ed: M. Vázquez), Woodhead Publishing, Sawston **2020**.

[93] O. M. Volkov, D. D. Sheka, Y. Gaididei, V. P. Kravchuk, U. K. Rößler, J. Fassbender, D. Makarov, *Sci. Rep.* **2018**, *8*, 866.

[94] R. C. T. da Costa, *Phys. Rev. A* **1981**, *23*, 1982.

[95] K. V. Yershov, V. P. Kravchuk, D. D. Sheka, Y. Gaididei, *Phys. Rev. B* **2015**, *92*, 104412.

[96] T. Moriya, *Phys. Rev. Lett.* **1960**, *4*, 228.

[97] S. Sternberg, *Curvature in Mathematics and Physics*, Dover Pubications, Mineola, NY **2012**.

[98] V. P. Kravchuk, U. K. Rößler, O. M. Volkov, D. D. Sheka, J. van den Brink, D. Makarov, H. Fuchs, H. Fangohr, Y. Gaididei, *Phys. Rev. B* **2016**, *94*, 144402.

[99] G. Gioia, R. D. James, *Proc. R. Soc. Lond., Ser. A* **1997**, *453*, 213.

[100] R. V. Kohn, V. V. Slastikov, *Arch. Ration. Mech. Anal.* **2005**, *178*, 227.

[101] V. Slastikov, *Math. Models Methods Appl. Sci.* **2005**, *15*, 1469.

[102] V. S. Tkachenko, A. N. Kuchko, M. Dvornik, V. V. Kruglyak, *Appl. Phys. Lett.* **2012**, *101*, 152402.

[103] M. Kläui, C. A. F. Vaz, L. Lopez-Diaz, J. A. C. Bland, *J. Phys.: Condens. Matter* **2003**, *15*, R985.

[104] A. P. Guimarães, *Principles of Nanomagnetism, NanoScience and Technology*, Springer-Verlag Berlin, Heidelberg **2009**.

[105] *NIST Handbook of Mathematical Functions* (Eds: F. W. J. Olver, D. W. Lozier, R. F. Boisvert, C. W. Clark), Cambridge University Press, New York, NY **2010**.

[106] K. V. Yershov, V. P. Kravchuk, D. D. Sheka, O. V. Pylypovskyi, D. Makarov, Y. Gaididei, *Phys. Rev. B* **2018**, *98*, 060409(R).

[107] J. C. Slonczewski, *Int. J. Magn.* **1972**, *2*, 85.

[108] A. A. Thiele, *Phys. Rev. Lett.* **1973**, *30*, 230.

[109] A. P. Malozemoff, J. C. Slonzewski, *Magnetic Domain Walls in Bubble Materials*, Academic Press, New York **1979**.

[110] O. M. Volkov, F. Kronast, I. Mönch, M.-A. Mawass, A. Kákay, J. Fassbender, D. Makarov, *Phys. Status Solidi - RRL* **2019**, *13*, 1800309.

[111] O. Boulle, J. Vogel, H. Yang, S. Pizzini, D. de Souza Chaves, A. Locatelli, T. O. Menteş, A. Sala, L. D. Buda-Prejbeanu, O. Klein, M. Belmeguenai, Y. Roussigné, A. Stashkevich, S. M. Chérif, L. Aballe, M. Foerster, M. Chshiev, S. Auffret, I. M. Miron, G. Gaudin, *Nat. Nanotechnol.* **2016**, *11*, 449.

[112] S. V. Grigoriev, S. V. Maleyev, V. A. Dyadkin, D. Menzel, J. Schoenes, H. Eckerlebe, *Phys. Rev. B* **2007**, *76*, 092407.

[113] H. Yang, A. Thiaville, S. Rohart, A. Fert, M. Chshiev, *Phys. Rev. Lett.* **2015**, *115*, 267210.

[114] V. P. Kravchuk, *J. Magn. Magn. Mater.* **2014**, *367*, 9.

[115] M. Yoneya, K. Kuboki, M. Hayashi, *Phys. Rev. B* **2008**, *78*, 064419.

[116] O. V. Pylypovskyi, V. P. Kravchuk, D. D. Sheka, D. Makarov, O. G. Schmidt, Y. Gaididei, *Phys. Rev. Lett.* **2015**, *114*, 197204.

[117] S. Mendach, J. Podbielski, J. Topp, W. Hansen, D. Heitmann, *Appl. Phys. Lett.* **2008**, *93*, 262501.

[118] F. Balhorn, S. Mansfeld, A. Krohn, J. Topp, W. Hansen, D. Heitmann, S. Mendach, *Phys. Rev. Lett.* **2010**, *104*, 037205.

[119] *Three-Dimensional Magnonics: Layered, Micro- and Nanostructures*, (Ed: G. Gubbiotti), 1st ed., Jenny Stanford Publishing, Singapore **2019**.

[120] G. Gubbiotti, A. Sadovnikov, E. Beginin, S. Sheshukova, S. Nikitov, G. Talmelli, I. Asselberghs, I. P. Radu, C. Adelmann, F. Ciubotaru, *Appl. Phys. Lett.* **2021**, *118*, 162405.

[121] O. V. Dobrovolskiy, N. R. Vovk, A. V. Bondarenko, S. A. Bunyaev, S. Lamb-Camarena, N. Zenbaa, R. Sachser, S. Barth, K. Y. Guslienko, A. V.Chumak, M. Huth, G. N. Kakazei, *Appl. Phys. Lett.* **2021**, *118*, 132405.

[122] A. Barman, G. Gubbiotti, S. Ladak, A. O. Adeyeye, M. Krawczyk, J. Gräfe, C. Adelmann, S. Cotofana, A. Naeemi, V. I. Vasyuchka, B. Hillebrands, S. A. Nikitov, H. Yu, D. Grundler, A. Sadovnikov, A. A. Grachev, S. E. Sheshukova, J.-Y. Duquesne, M. Marangolo, C. Gyorgy, W. Porod, V. E. Demidov, S. Urazhdin, S. Demokritov, E. Albisetti, D. Petti, R. Bertacco, H. Schulteiss, V. V. Kruglyak, V. D. Poimanov, et al., *J. Phys.: Condens. Matter* **2021**.

[123] K. Vogt, H. Schultheiss, S. Jain, J. E. Pearson, A. Hoffmann, S. D. Bader, B. Hillebrands, *Appl. Phys. Lett.* **2012**, *101*, 042410.

[124] V. S. Tkachenko, A. N. Kuchko, V. V. Kruglyak, *Low Temp. Phys.* **2013**, *39*, 163.

[125] I. Turčan, L. Flajšman, O. Wojewoda, V. Roučka, O. Man, M. Urbánek, *Appl. Phys. Lett.* **2021**, *118*, 092405.

[126] D. D. Sheka, I. A. Yastremsky, B. A. Ivanov, G. M. Wysin, F. G. Mertens, *Phys. Rev. B* **2004**, *69*, 054429.

[127] C. Kittel, *Introduction to Solid State Physics*, 8th ed., Wiley, New York **2005**.

[128] K. Zakeri, Y. Zhang, J. Prokop, T.-H. Chuang, N. Sakr, W. X. Tang, J. Kirschner, *Phys. Rev. Lett.* **2010**, *104*, 137203.

[129] D. Cortes-Ortuno, P. Landeros, *J. Phys.: Condens. Matter* **2013**, *25*, 156001.

[130] K. Zakeri, *Phys. Rep.* **2014**, *545*, 47.

[131] A. González, P. Landeros, Álvaro S. Núñez, *J. Magn. Magn. Mater.* **2010**, *322*, 530.

[132] J.-S. Kim, M.-A. Mawass, A. Bisig, B. Krüger, R. M. Reeve, T. Schulz, F. Büttner, J. Yoon, C.-Y. You, M. Weigand, H. Stoll, G. Schütz, H. J. M. Swagten, B. Koopmans, S. Eisebitt, M. Kläui, *Nat. Commun.* **2014**, *5*, 3429.

[133] Spin Dynamics in Confined Magnetic Structures III (Eds: B. Hillebrands, A. Thiaville), vol. 101 of Topics in Applied Physics, Springer, Berlin, Heidelberg 2006.

[134] A. Thiaville, Y. Nakatani, J. Miltat, Y. Suzuki, Europhys. Lett. 2005, 69, 990.

[135] Y. B. Bazaliy, B. A. Jones, S.-C. Zhang, Phys. Rev. B 1998, 57, R3213.

[136] S. Zhang, Z. Li, Phys. Rev. Lett. 2004, 93, 127204.

[137] A. Mougin, M. Cormier, J. P. Adam, P. J. Metaxas, J. Ferré, Europhys. Lett. 2007, 78, 57007.

[138] J.-Y. Chauleau, R. Weil, A. Thiaville, J. Miltat, Phys. Rev. B 2010, 82, 214414.

[139] K. Richter, A. Krone, M.-A. Mawass, B. Krüger, M. Weigand, H. Stoll, G. Schütz, M. Kläui, Phys. Rev. B 2016, 94, 024435.

[140] M.-A. Mawass, K. Richter, A. Bisig, R. M. Reeve, B. Krüger, M. Weigand, H. Stoll, A. Krone, F. Kronast, G. Schütz, M. Kläui, Phys. Rev. Appl. 2017, 7, 044009.

[141] V. Brajuskovic, C. Phatak, Appl. Phys. Lett. 2021, 118, 152409.

[142] A. V. Khvalkovskiy, V. Cros, D. Apalkov, V. Nikitin, M. Krounbi, K. A. Zvezdin, A. Anane, J. Grollier, A. Fert, Phys. Rev. B 2013, 87, 020402.

[143] J. Sinova, S. O. Valenzuela, J. Wunderlich, C. H. Back, T. Jungwirth, Rev. Mod. Phys. 2015, 87, 1213.

[144] K. Obata, G. Tatara, Phys. Rev. B 2008, 77, 214429.

[145] Y. Tserkovnyak, A. Brataas, G. E. Bauer, J. Magn. Magn. Mater. 2008, 320, 1282.

[146] O. Volkov, U. K. Rossler, J. Fassbender, D. Makarov, J. Phys. D: Appl. Phys. 2019, 52, 345001.

[147] S.-C. Yang, A. Kumar, V. Petkov, S. Priya, J. Appl. Phys. 2013, 113, 144101.

[148] Y. Jia, S. W. Or, H. L. W. Chan, X. Zhao, H. Luo, Appl. Phys. Lett. 2006, 88, 242902.

[149] Y.-W. Liu, Q.-F. Zhan, R.-W. Li, Chin. Phys. B 2013, 22, 127502.

[150] P. Sheng, B. Wang, R. Li, J. Semicond. 2018, 39, 011006.

[151] G. S. C. Bermúdez, D. Makarov, Adv. Funct. Mater. 2021, 2007788.

[152] Y. Kim, H. Yuk, R. Zhao, S. A. Chester, X. Zhao, Nature 2018, 558, 274.

[153] W. Hu, G. Z. Lum, M. Mastrangeli, M. Sitti, Nature 2018, 554, 81.

[154] X. Wang, G. Mao, J. Ge, M. Drack, G. S. C. Bermúdez, D. Wirthl, R. Illing, T. Kosub, L. Bischoff, C. Wang, J. Fassbender, M. Kaltenbrunner, D. Makarov, Commun. Mater. 2020, 1, 67.

[155] M. Ha, G. S. C. Bermúdez, J. A.-C. Liu, E. S. O. Mata, B. A. Evans, J. B. Tracy, D. Makarov, Adv. Mater. 2021, 33, 2008751.

[156] J. A.-C. Liu, J. H. Gillen, S. R. Mishra, B. A. Evans, J. B. Tracy, Sci. Adv. 2019, 5, eaaw2897.

[157] H. Lu, M. Zhang, Y. Yang, Q. Huang, T. Fukuda, Z. Wang, Y. Shen, Nat. Commun. 2018, 9, 3944.

[158] B. J. Nelson, I. K. Kaliakatsos, J. J. Abbott, Annu. Rev. Biomed. Eng. 2010, 12, 55.

[159] M. Medina-Sánchez, V. Magdanz, M. Guix, V. M. Fomin, O. G. Schmidt, Adv. Funct. Mater. 2018, 28, 1707228.

[160] C. Hu, S. Pané, B. J. Nelson, Annu. Rev. Control, Robot., Autonom. Syst. 2018, 1, 53.

[161] H. Ceylan, I. C. Yasa, O. Yasa, A. F. Tabak, J. Giltinan, M. Sitti, ACS Nano 2019, 13, 3353.

[162] P. Bujak, I. Kulszewicz-Bajer, M. Zagorska, V. Maurel, I. Wielgus, A. Pron, Chem. Soc. Rev. 2013, 42, 8895.

[163] L. D. Landau, E. M. Lifshitz, Theory of Elasticity: v.7 (Course of Theoretical Physics), Pergamon Press, Oxford, NY 1981.

[164] D. Koks, Explorations in Mathematical Physics: The Concepts Behind an Elegant Language, Springer, New York 2006.

[165] D. A. Kitchaev, I. J. Beyerlein, A. Van der Ven, Phys. Rev. B 2018, 98, 214414.

[166] N. Challab, F. Zighem, D. Faurie, M. Haboussi, M. Belmeguenai, P. Lupo, A. O. Adeyeye, Phys. Status Solidi - RRL 2018, 13, 1800509.

[167] N. Challab, A. D. Aboumassound, F. Zighem, D. Faurie, M. Haboussi, J. Phys. D: Appl. Phys. 2019, 52, 355004.

[168] N. Challab, D. Faurie, M. Haboussi, F. Zighem, Phys. Status Solidi - RRL 2021, 15, 2100149.

[169] N. Challab, D. Faurie, M. Haboussi, A. O. Adeyeye, F. Zighem, ACS Appl. Mater. Interfaces 2021, 13, 29906.

[170] F. Vanderveken, J. Mulkers, J. Leliaert, B. V. Waeyenberge, B. Sorée, O. Zografos, F. Ciubotaru, C. Adelmann, Open Res. Eur. 2021, 1, 35.

[171] O. V. Pylypovskyi, Y. A. Borysenko, J. Fassbender, D. D. Sheka, D. Makarov, Appl. Phys. Lett. 2021, 118, 182405.

[172] T. H. Kim, S. H. Han, B. K. Cho, Commun. Phys. 2019, 2, 1.

[173] H. Y. Yuan, M.-H. Yung, X. R. Wang, Phys. Rev. Res. 2019, 1, 033052.

[174] K. Pan, L. Xing, H. Y. Yuan, W. Wang, Phys. Rev. B 2018, 97, 184418.

[175] F. Chen, Z. Zhang, W. Luo, X. Yang, L. You, Y. Zhang, J. Magn. Magn. Mater. 2020, 511, 166995.

[176] D. Makarov, M. Melzer, D. Karnaushenko, O. G. Schmidt, Appl. Phys. Rev. 2016, 3, 011101.

[177] D. Karnaushenko, T. Kang, O. G. Schmidt, Adv. Mater. Technol. 2019, 4, 1800692.

[178] M. Melzer, D. Makarov, O. G. Schmidt, J. Phys. D: Appl. Phys. 2020, 53, 083002.

[179] I. Mönch, D. Makarov, R. Koseva, L. Baraban, D. Karnaushenko, C. Kaiser, K.-F. Arndt, O. G. Schmidt, ACS Nano 2011, 5, 7436.

[180] J. Schumann, K. G. Lisunov, W. Escoffier, B. Raquet, J. M. Broto, E. Arushanov, I. Mönch, D. Makarov, C. Deneke, O. G. Schmidt, Nanotechnology 2012, 23, 255701.

[181] R. Streubel, D. Makarov, J. Lee, C. Müller, M. Melzer, R. Schäfer, C. C. B. Bufon, S.-K. Kim, O. G. Schmidt, SPIN 2013, 03, 1340001.

[182] R. Streubel, J. Lee, D. Makarov, M.-Y. Im, D. Karnaushenko, L. Han, R. Schäfer, P. Fischer, S.-K. Kim, O. G. Schmidt, Adv. Mater. 2014, 26, 316.

[183] D. Karnaushenko, D. D. Karnaushenko, D. Makarov, S. Baunack, R. Schäfer, O. G. Schmidt, Adv. Mater. 2015, 27, 6582.

[184] Y. Dong, L. Cai, T. Xu, H.-A. Zhou, W. Jiang, Appl. Phys. Lett. 2021, 118, 212406.

[185] J. Grollier, D. Querlioz, K. Y. Camsari, K. Everschor-Sitte, S. Fukami, M. D. Stiles, Nat. Electron. 2020, 3, 360.

[186] M. Sitti, Mobile Microrobotics, MIT Press, Cambridge, MA 2017.

[187] Y. Alapan, O. Yasa, B. Yigit, I. C. Yasa, P. Erkoc, M. Sitti, Annu. Rev. Control, Robot., Autonom. Syst. 2019, 2, 205.

[188] M. Medina-Sánchez, O. G. Schmidt, Nature 2017, 545, 406.

Denis D. Sheka received his Ph.D. degree from the Institute of Magnetism (Kyiv, Ukraine, 1995) and work in positions of assistant/associate/full professor at the Taras Shevchenko National University of Kyiv (KNU). He received a D.Sci. degree in theoretical physics from Bogolyubov Institute for Theoretical Physics (Kyiv, Ukraine, 2009). Since 2013 he is a full Professor at KNU being a leading specialist in the theory of nonlinear phenomena in nanomagnets and theory of curvilinear magnetism.

Oleksandr V. Pylypovskyi received his Ph.D. in 2016 from Bogolyubov Institute for Theoretical Physics (Kyiv, Ukraine) and worked as an assistant professor at the Taras Shevchenko National University of Kyiv. At present, he is a researcher at the Helmholtz-Zentrum Dresden-Rossendorf (Dresden, Germany) and a lecturer at the Kyiv Academic University (Kyiv, Ukraine). His main research interests include properties of magnetic solitons in ferro- and antiferromagnetic materials, phenomena in curvilinear magnetic geometries, and numerical techniques in magnetism.

Oleksii M. Volkov obtained his Ph.D. degree in 2015 from the Bogolyubov Institute for Theoretical Physics of National Academy of Sciences of Ukraine (Kyiv, Ukraine), where he worked as a junior researcher. Since 2016 he is working as a researcher at the Helmholtz-Zentrum Dresden-Rossendorf (Dresden, Germany). The main research interests include fundamental investigations of topologically non-trivial magnetic textures in geometrically curved low dimensional ferromagnets. His research activities are supported by the German Research Foundation (DFG).

Kostiantyn V. Yershov obtained his Ph.D. (2017) from the Bogolyubov Institute for Theoretical Physics (Kyiv, Ukraine), where he worked as a junior researcher. At present, he is a researcher at the Leibniz Institute for Solid State and Materials Research (Dresden, Germany). His main research interests include geometry-induced effects in statics and dynamics of anti- and ferromagnetic topological solitons, and magnetization-induced shape transformations of magnetoelastic systems.

ADVANCED
SCIENCE NEWS
www.advancedsciencenews.com

NANO · MICRO
small
www.small-journal.com

Volodymyr P. Kravchuk obtained Ph.D. in theoretical physics (2009) from Bogolyubov Institute of Theoretical Physics (BITP) in Kyiv, Ukraine. From 2016 until 2018, he was at the Leibniz IFW Dresden with a Humboldt scholarship for experienced researchers. Currently, he is a postdoc at the Karlsruhe Institute of Technology and senior researcher at BITP. His area of interest is analytical micromagnetism applied to topological magnetic solitons (skyrmions, merons, domain walls) in curved geometries, dynamics of skyrmion strings, chaos in nonlinear magnetic systems, spectral properties and nonlinear dynamics of ordered topological magnetic states such as lattices of skyrmions and merons.

Denys Makarov received his Ph.D. (2008) from the University of Konstanz, Germany. Currently, he is head of department "Intelligent materials and systems" at the Helmholtz-Zentrum Dresden-Rossendorf and leads the Helmholtz Innovation Lab FlexiSens. With his activities, Denys Makarov made a decisive contribution to the development of the field of curvilinear magnetism and stimulated research on mechanically flexible, printable and skin-conformal magnetoelectronics for human-machine interfaces, soft robotics, eMobility and medicine. These activities are supported via major national and European projects. Denys Makarov is Senior Member of the IEEE and Fellow of the Young Academy of Europe.